Computers and Fluids 202 (2020) 104492

Contents lists available at ScienceDirect

Computers and Fluids

journal homepage: www.elsevier.com/locate/compfluid

Rectangular lattice Boltzmann method using multiple relaxation time collision operator in two and three dimensions

Vanja Zecevic*, Michael P. Kirkpatrick, Steven W. Armfield

School of Aerospace, Mechanical and Mechatronic Engineering – The University of Sydney, NSW 2006, Australia

ARTICLE INFO

Article history:
Received 7 August 2019
Revised 26 November 2019
Accepted 28 February 2020
Available online 29 February 2020

Keywords:
Lattice Boltzmann method
Rectangular grid
Turbulent channel flow
Multiple relaxation time collision operator
GPUcomputing
Linear stability analysis

ABSTRACT

We present a lattice Boltzmann (LB) method using a rectangular, non-isotropic lattice based on D2Q9 and D3Q27 velocity sets in two and three dimensions. A second order multi-scale expansion ensures that the scheme correctly reproduces hydrodynamic behaviour. A novel set of basis vectors is introduced in order to allow independent adjustment of eigenvalues corresponding to second order moments as required in order to ensure correct hydrodynamic behaviour using the non-isotropic lattice. Errors are reduced compared to other rectangular grid implementations. Linear perturbation analysis indicates that our scheme has similar stability properties to the isotropic LB method. We investigate the error behaviour of our scheme by performing Taylor-Green vortex flow simulations and comparing our results to simulations using a square grid and also to analytical results. We demonstrate that our scheme is well suited to direct numerical simulation of wall bounded turbulent flows and compare to well known benchmark results.

1. Introduction

The lattice Boltzmann (LB) method has been increasing in popularity as a means of simulating fluid flow. The explicit and local nature of calculations allows highly efficient parallel implementations and the method has been successfully adapted to massively parallel computing architectures such as graphics processing units [1–4] as well as achieving high performance on traditional parallel machines [5–7]. The kinetic nature of the LB method simplifies the implementation of additional physics and the method has enjoyed success in simulating flows involving multiple phases or components, reacting species and complex geometries such as porous media as well as particle laden flows, thermal flows and microfluidics. Thorough reviews of the method and its application to the range of problems mentioned, as well as incompressible and compressible fluid dynamics are presented in Annual Reviews [8,9] and books [10,11].

Despite these successes, one persistent drawback has been that the standard lattice Boltzmann method relies on a uniform, square or cube shaped grid coinciding with an isotropic velocity basis so that the advection part of the discrete velocity Boltzmann equation,

$$\partial_t f_i(x_\beta, t) + c_{i\alpha}\partial_\alpha f_i(x_\beta, t) = \Omega_i(x_\beta, t),$$

may be solved by simple point to point transfer of particles. To date, most progress towards the use of non-uniform grids has been made by retaining the isotropic velocity basis and performing calculations on an unrelated, non-uniform computational grid. The advection of particles can be solved using finite volume methods [6,12–14], finite element methods [15–18], or finite difference methods [19–21]. Spectral schemes have also been used [22]. Decoupling the grid from the velocity basis even allows the use of velocity basis that does not tile space, such as the 13 velocity, icosahedral basis used by Tamura et al. [21]. Second order or higher difference schemes must be used in order to avoid introducing numerical viscosity, resulting in additional stability concerns compared to the unconditionally stable point to point advection of the normal LB method. Stability can be ensured for finite volume schemes by using flux limiters [6] while others have simply reported reduced stability and the presence of oscillations as drawbacks of their proposed schemes [21].

Standard LB methods use an upwind collision operator, where the collision term is calculated and applied at the beginning of the time step, followed by an independent streaming operation. This decoupling of advection and collision terms introduces an artificial negative viscosity which is related to the grid size and time step and is also referred to as the discrete lattice effect. Thus when the grid is non-uniform, the upwind collision operator may not be used since the discrete lattice effect would vary across the domain and the collision operator must then be solved using a higher order scheme, which must also take into account the interdependent effects of particle advection and collision. Ubertini,

* Corresponding author.
E-mail address: vanja.zecevic@sydney.edu.au (V. Zecevic).

https://doi.org/10.1016/j.compfluid.2020.104492
0045-7930/

Succi and Bella [14] have noted issues in reaching a small viscosity while other studies have not tested the stability at small viscosities [12,13,19]. Advanced treatments of the collision operator have been proposed [15–18,20] and have demonstrated success with higher Reynolds number unsteady flows, although these methods have thus far only been demonstrated in two dimensions.

The interpolation supplemented LB method [23–27] is an alternative approach keeping simple point to point advection of particles and an upwind collision operator. Particle locations no longer coincide with grid points after advection so interpolation is used to reconstruct the populations at grid sites. Second order or higher interpolation must be used in order to maintain the second order accuracy of the LB method and results can be improved by using a least squares interpolation [26,27]. These methods have had success at higher Reynolds numbers, however they require significant additional computational effort and introduce additional stability concerns.

Another alternative to these methods is to use local grid refinement, using smaller cube elements [5,28–30]. Grid refinement does not allow the treatment of curved boundaries or the use of non-rectangular elements as the other mentioned methods do however it has been shown to successfully simulate fully turbulent three dimensional flows [5,31].

All of these methods introduce significant additional computational effort and complexity and some of them suffer from reduced stability. Karlin, Succi and Orszag Karlin et al. [32] were the first to suggested a lattice Boltzmann method on a completely irregular grid but noted that there were significant problems to be solved before it would become usable. Lattice Boltzmann schemes using a non-isotropic but uniform rectangular grid and corresponding velocities basis such that particle populations transfer directly from one node to another, have since been implemented. The generalised LB method, also known as the multiple relaxation time (MRT) method, simplifies implementation of these schemes since it is sufficient to define equilibrium moments rather than an explicit formula for each equilibrium population.

The standard D2Q9 MRT lattice can reproduce the correct hydrodynamic moments up to second order. Bouzidi et al. [33] introduced a two dimensional scheme based on the D2Q9 lattice using this approach noting stability decreases as the aspect ratio of each cell was increased from one. Zhou [34,35], Ren et. al. [36] and Hegeler et. al. [37] have also demonstrated similar schemes however the aforementioned models do not correctly model diffusive terms since the third order and higher moments are not hydrodynamically correct and hence viscosity is not isotropic. Adjusting the relaxation rates alone is not sufficient to recover hydrodynamic behaviour using the standard velocity basis.

Peng et. al. [38] have developed a MRT based LB method which correctly reproduces hydrodynamic behaviour. The errors introduced by incorrect rank three moments previously mentioned are corrected by using a quasi-equilibrium collision operator. Peng et. al. perform a multi-scale expansion based on each moment that is used as a basis in order to develop the coefficients that are used in the quasi-equilibrium terms. As a consequence, the analysis must be repeated in order to develop coefficients for each new lattice that may be developed in the future. Results are presented for the D2Q9 velocity set using the He and Luo [39] incompressible approximation.

In this paper we present a novel rectangular lattice Boltzmann method including two and three dimensional lattices as shown in Fig. 1. Our method uses a different set of basis vectors compared to typical MRT methods that allows hydrodynamic behaviour to be restored by adjusting relaxation parameters alone without requiring any quasi-equilibrium collision step. Both our work and the work of Peng et. al. [38] correctly eliminates all diffusive errors in the second order multi-scale expansion however our work is also extended to three dimensions. Our theoretical derivation is based on the standard multi-scale expansion typically applied to LB methods rather than the perturbation analysis or moment based analysis used by Peng et. al., which means that our method is applicable to a larger range of lattices without requiring extensive recalculation of coefficients. Our analysis is also novel since it does not use the He and Luo [39] incompressible approximation during multi-scale expansion.

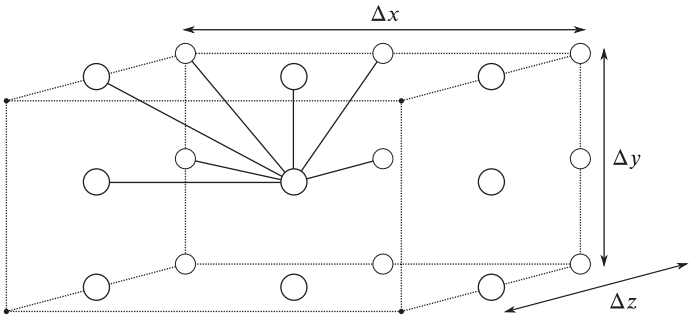

Fig. 1. Non-isotropic unit cell showing subset of D3Q27 velocity vectors.

We perform a linear perturbation analysis and find that the maximum stable Mach number decreases if the aspect ratio is increased in the same direction as the mean flow. The scheme retains similar stability compared to uniform grid methods for moderate aspect ratios. This instability is sensitive to the flow being investigated and will be more problematic for configurations with a significant mean velocity. The D3Q27 lattice used has a chequerboard invariant that can cause stability problems in some situations [40–42]. We have successfully used fractional propagation to eliminate this problem. Adjustment of relaxation rates corresponding to non-hydrodynamic moments has been reported as a means of stabilising LB simulations [41,43] although we have not found it necessary to use this stabilization method in our turbulent calculations.

Our scheme is tested for convergence by comparing to the analytic solutions of Taylor-Green vortex flow with varying Mach number and grid resolution. We perform a direct numerical simulation of turbulent channel flow using both normal and non-isotropic grids and compare turbulence statistics to the results of Moser et al. [44], finding good agreement between LB simulations using isotropic and rectangular grids.

The use of a non-isotropic grid allows improvements in computational efficiency for flow configurations that have larger gradients in one direction. The advantage of the present scheme, compared to other methods capable of using a fully non-uniform grid, is in its simplicity. The scheme does not introduce any new calculation steps or theoretical assumptions compared to the well understood MRT method. Research on the use of non-isotropic lattices is also important because it will advance progress towards the use of a fully non-uniform lattice Boltzmann method [32].

2. Lattice Boltzmann method

Most common lattice Boltzmann methods, including the single relaxation time method and the generalised LB method can be described using a linear collision operator [45]. We have included a slightly more general form than usual using a non-unit Courant number (Cr) for particle advection [46],

$$Cr = \frac{||c_{i\alpha}||\Delta t}{||\Delta x_\alpha||}.$$

The time advancement of these methods is,

$$f_{\boldsymbol{i}}(x_\alpha + \Delta x_\alpha, t + \Delta t) = (1 - Cr) f_{\boldsymbol{i}}(x_\alpha + \Delta x_\alpha, t) + Cr f_{\boldsymbol{i}}(x_\alpha, t) + \Delta t \Omega_{\boldsymbol{i}}(x_\alpha, t), \tag{1}$$

where Ω is the linearised collision operator,

$$\Omega_{\boldsymbol{i}}(x_\alpha, t) = \sum_{\boldsymbol{j}=0}^{q} A_{\boldsymbol{ij}}\left(f_{\boldsymbol{j}}(x_\alpha, t) - f_{\boldsymbol{j}}^{eq}(x_\alpha, t)\right). \tag{2}$$

Here bold Roman subscripts represent particle populations with no implied summation and Greek subscripts represent Cartesian directions with implied summation over repeated indices. The single relaxation time method assumes that the collision matrix A is the identity matrix multiplied by some constant relaxation factor, $A = -\omega I$. Using a multi-scale expansion as introduced by Frisch et al. [47], we show in Appendix A that these methods approach the incompressible Navier-Stokes equations with errors proportional to the Mach number squared,

$$\partial_\alpha \rho u_\alpha = \mathcal{O}\left(\mathrm{Ma}^2\right), \tag{3a}$$

$$\partial_t \rho u_\alpha + \partial_\beta \rho u_\alpha u_\beta = -\partial_\alpha P + \nu \rho \partial_\beta \partial_\beta u_\alpha + \mathcal{O}\left(\mathrm{Ma}^2\right). \tag{3b}$$

Here the pressure is approximated by an artificially compressible density field, $P = \rho c_s^2$. The equilibrium moments up to second order are required to take the following values, which are equal to the equilibrium moments of the Maxwell-Boltzmann distribution:

$$\sum_{\boldsymbol{i}=0}^{q} f_{\boldsymbol{i}} = \sum_{\boldsymbol{i}=0}^{q} f_{\boldsymbol{i}}^{eq} = \rho, \tag{4a}$$

$$\sum_{\boldsymbol{i}=0}^{q} c_{\boldsymbol{i}\alpha} f_{\boldsymbol{i}} = \sum_{\boldsymbol{i}=0}^{q} c_{\boldsymbol{i}\alpha} f_{\boldsymbol{i}}^{eq} = \rho u_\alpha, \tag{4b}$$

$$\sum_{\boldsymbol{i}=0}^{q} c_{\boldsymbol{i}\alpha} c_{\boldsymbol{i}\beta} f_{\boldsymbol{i}}^{eq} = c_s^2 \delta_{\alpha\beta} \rho + \rho u_\alpha u_\beta. \tag{4c}$$

In the following section we will discuss the requirements to correctly recover the viscous terms in the Navier-Stokes momentum equations.

2.1. Correct viscosity

Correct hydrodynamic behaviour can be achieved by also setting higher order equilibrium moments so that they are equal to corresponding equilibrium moments of the Maxwell-Boltzmann distribution. Due to linear dependence between moments, some commonly used velocity basis sets including the D2Q9 and D3Q27 sets do not allow setting the third order equilibrium moments to the correct value and the velocity cubed term in Eq. (A.23) must be dropped. The following form is used,

$$\sum_{\boldsymbol{i}=0}^{q} c_{\boldsymbol{i}\alpha} c_{\boldsymbol{i}\beta} c_{\boldsymbol{i}\gamma} f_{\boldsymbol{i}}^{eq} = c_s^2 \left(\delta_{\alpha\delta}\delta_{\beta\gamma} + \delta_{\alpha\beta}\delta_{\gamma\delta} + \delta_{\alpha\gamma}\delta_{\beta\delta}\right) \rho u_\delta. \tag{5}$$

As shown in Appendix A, this is sufficient to correctly model the incompressible Navier-Stokes equations (Eq. (3)) in the small Mach number limit.

Another crucial assumption is that multiplication of the second order moments by the collision matrix is equivalent to scalar multiplication. This is true for single relaxation time methods because the collision matrix is proportional to the identity matrix and it is also true for the generalised LB method because the second order sums are eigenvectors of the collision matrix,

$$\sum_{\boldsymbol{j}=0}^{q} A_{\boldsymbol{ij}}^{-1} c_{\boldsymbol{j}\alpha} c_{\boldsymbol{j}\beta} = \frac{1}{\lambda_0} c_{\boldsymbol{i}\alpha} c_{\boldsymbol{i}\beta}. \tag{6}$$

The viscosity, as shown in Appendix A is equal to,

$$\nu = -c_s^2 \left(\frac{\Delta t}{2Cr} + \frac{1}{\lambda_0}\right). \tag{7}$$

We now show that it is possible to correctly model viscosity even if the third order sums take the more general, non-isotropic form.

We introduce the following rank two tensors;

$$d_{\alpha\beta}^{sq} = \begin{pmatrix} \Delta x^2 & 0 & 0 \\ 0 & \Delta y^2 & 0 \\ 0 & 0 & \Delta z^2 \end{pmatrix}, \; \lambda_{\alpha\beta}^{-1} = \begin{pmatrix} \lambda_{xx}^{-1} & 0 & 0 \\ 0 & \lambda_{yy}^{-1} & 0 \\ 0 & 0 & \lambda_{zz}^{-1} \end{pmatrix}. \tag{8}$$

We also generalise these to diagonal rank four tensors,

$$\left.\begin{aligned} d_{\alpha\beta\gamma\delta}^{sq} &= d_{\alpha\beta}^{sq} \\ \lambda_{\alpha\beta\gamma\delta}^{-1} &= \lambda_{\alpha\beta}^{-1} \end{aligned}\right\} \quad \text{if} \quad \alpha = \beta = \gamma = \delta. \tag{9}$$

and zero otherwise. The third order sums now take the form,

$$\sum_{\boldsymbol{i}=} 0^q c_{\boldsymbol{i}\alpha} c_{\boldsymbol{i}\beta} c_{\boldsymbol{i}\gamma} f_{\boldsymbol{i}}^{eq} = \Big[c_s^2 \left(\delta_{\alpha\beta}\delta_{\gamma\delta} + \delta_{\alpha\gamma}\delta_{\beta\delta} + \delta_{\alpha\delta}\delta_{\beta\gamma}\right) - 3c_s^2 \delta_{\alpha\beta\gamma\delta} + d_{\alpha\beta\gamma\delta}^{sq} \Big] \rho u_\delta. \tag{10}$$

Eigenvalues λ_{xx}, corresponding to eigenvectors $c_{\boldsymbol{i}x} c_{\boldsymbol{i}x}$ are now allowed to be different to λ_0,

$$\sum_{\boldsymbol{j}=0}^{q} A_{\boldsymbol{ij}}^{-1} c_{\boldsymbol{j}\alpha} c_{\boldsymbol{j}\beta} = \lambda_0^{-1} c_{\boldsymbol{i}\alpha} c_{\boldsymbol{i}\beta} + \left(\lambda_{\alpha\beta\epsilon\zeta}^{-1} - \lambda_0^{-1} \delta_{\alpha\beta\epsilon\zeta}\right) c_{\boldsymbol{i}\epsilon} c_{\boldsymbol{i}\zeta}. \tag{11}$$

The low Mach number simplified form of Eq. (A.21) becomes,

$$\partial_{t_2} \rho u_\alpha + \left(\frac{\Delta t}{2Cr} + \lambda_0^{-1}\right) \partial_\beta \partial_\gamma \sum_{\boldsymbol{i}=0}^{q} c_{\boldsymbol{i}\alpha} c_{\boldsymbol{i}\beta} c_{\boldsymbol{i}\gamma} f_{\boldsymbol{i}}^{eq} + \partial_\beta \partial_\gamma \sum_{\boldsymbol{i}=0}^{q} c_{\boldsymbol{i}\epsilon} c_{\boldsymbol{i}\zeta} c_{\boldsymbol{i}\gamma} f_{\boldsymbol{i}}^{eq} \left(\lambda_{\alpha\beta\epsilon\zeta}^{-1} - \lambda_0^{-1} \delta_{\alpha\beta\epsilon\zeta}\right) = \mathcal{O}\left(\mathrm{Ma}^2\right).$$

Expanding the more complicated third order moments gives,

$$\begin{aligned} \partial_{t_2} \rho u_\alpha + c_s^2 \left(\frac{\Delta t}{2Cr} + \lambda_0^{-1}\right) \rho \partial_\beta \partial_\beta u_\alpha \\ + \partial_\beta \partial_\gamma \Bigg[\left(\frac{\Delta t}{2Cr} + \lambda_0^{-1}\right) \left(d_{\alpha\beta\gamma\delta}^{sq} - 3c_s^2 \delta_{\alpha\beta\gamma\delta}\right) \\ + c_s^2 \left(\delta_{\epsilon\zeta}\delta_{\gamma\delta} + \delta_{\epsilon\delta}\delta_{\gamma\zeta} + \delta_{\epsilon\gamma}\delta_{\zeta\delta}\right) \left(\lambda_{\alpha\beta\epsilon\zeta}^{-1} - \lambda_0^{-1}\delta_{\alpha\beta\epsilon\zeta}\right) \\ + \left(\lambda_{\alpha\beta\epsilon\zeta}^{-1} - \lambda_0^{-1}\delta_{\alpha\beta\epsilon\zeta}\right) \left(d_{\epsilon\zeta\gamma\delta}^{sq} - 3c_s^2 \delta_{\epsilon\zeta\gamma\delta}\right) \Bigg] \rho u_\delta \\ = \mathcal{O}\left(\mathrm{Ma}^2\right). \end{aligned}$$

After simplification of the fourth rank terms,

$$\begin{aligned} \partial_{t_2} \rho u_\alpha + c_s^2 \left(\frac{\Delta t}{2Cr} + \lambda_0^{-1}\right) \rho \partial_\beta \partial_\beta u_\alpha + c_s^2 \lambda_{\alpha\beta}^{-1} \partial_\beta \partial_\gamma \rho u_\gamma \\ + \partial_\beta \partial_\gamma \Bigg[\left(\frac{\Delta t}{2Cr} + \lambda_0^{-1}\right) \left(d_{\alpha\beta\gamma\delta}^{sq} - 3c_s^2 \delta_{\alpha\beta\gamma\delta}\right) \\ + 2c_s^2 \left(\lambda_{\alpha\beta\gamma\delta}^{-1} - \lambda_0^{-1}\delta_{\alpha\beta\gamma\delta}\right) \\ + \left(\lambda_{\alpha\beta\epsilon\zeta}^{-1} - \lambda_0^{-1}\delta_{\alpha\beta\epsilon\zeta}\right) \left(d_{\epsilon\zeta\gamma\delta}^{sq} - 3c_s^2 \delta_{\epsilon\zeta\gamma\delta}\right) \Bigg] \rho u_\delta \\ = \mathcal{O}\left(\mathrm{Ma}^2\right). \end{aligned}$$

Simplifying gives the following form for the momentum equation at order ϵ^2,

$$\partial_{t_2}\rho u_\alpha + c_s^2\left(\frac{\Delta t}{2Cr}+\lambda_0^{-1}\right)\rho\partial_\beta\partial_\beta u_\alpha + \partial_\beta\partial_\gamma\left[2c_s^2\left(\lambda^{-1}_{\alpha\beta\gamma\delta}-\lambda_0^{-1}\delta_{\alpha\beta\gamma\delta}\right)\right.$$
$$\left.+\left(\frac{\Delta t}{2Cr}\delta_{\alpha\beta\epsilon\zeta}+\lambda^{-1}_{\alpha\beta\epsilon\zeta}\right)\left(d^{sq}_{\epsilon\zeta\gamma\delta}-3c_s^2\delta_{\epsilon\zeta\gamma\delta}\right)\right]\rho u_\delta = \mathcal{O}\left(\mathrm{Ma}^2\right). \tag{12}$$

The contribution from rank four terms in the x direction are set to zero,

$$\left(\frac{\Delta t}{2Cr}+\lambda_{xx}^{-1}\right)\left(\Delta x^2-3c_s^2\right)+2c_s^2\left(\lambda_{xx}^{-1}-\lambda_0^{-1}\right)=0.$$

Thus, the correct value for eigenvalues corresponding to eigenvectors $c_{\mathbf{i}x}c_{\mathbf{i}x}$ must be,

$$\boxed{\lambda_{xx}=\frac{\Delta x^2-c_s^2}{2\frac{c_s^2}{\lambda_0}+\frac{\Delta t}{2Cr}\left(3c_s^2-\Delta x^2\right)}} \tag{13}$$

and similarly for other directions. The shear viscosity is not changed,

$$\boxed{\nu=-c_s^2\left(\frac{\Delta t}{2Cr}+\frac{1}{\lambda_0}\right)}. \tag{14}$$

This result reduces to the commonly used single relaxation time method if the Courant number, grid size and time step are all one, $\lambda_0=-\omega$ and $c_s^2=1/3$.

2.2. Multiple relaxation time lattice Boltzmann method

Lallemand and Luo proposed the moment based multiple relaxation time (MRT) LB method in 2000 [41]. The collision operator is rewritten in terms of an orthogonal basis set with judiciously chosen basis vectors that match the terms appearing in the multi-scale expansion summarised at the start of this section. Lallemand and Luo analysed the transport coefficients of small perturbations rather than performing multi-scale expansion in order to prove hydrodynamic behaviour.

The evolution equation for the moment based method is,

$$f_{\mathbf{i}}(x_\alpha+\Delta x_\alpha, t+\Delta t)=f_{\mathbf{i}}(x_\alpha,t)+M^{-1}_{\mathbf{il}}S_{\mathbf{lk}}\left[m_{\mathbf{k}}(x_\alpha,t)-m^{eq}_{\mathbf{k}}(x_\alpha,t)\right]. \tag{15}$$

This simplifies analysis because the equilibrium moments from Eq. (4) are set directly. The rows of matrix M are the basis vectors $\psi_{\mathbf{i}}$ relating moments $m_{\mathbf{j}}$ to the particle distributions,

$$m_{\mathbf{j}}=\sum_{\mathbf{i}=0}^{q}M_{\mathbf{ij}}f_{\mathbf{i}}.$$

The collision matrix A is represented as an eigen-decomposition where the columns of M^T are eigenvectors of A and S is a diagonal matrix of eigenvalues,

$$A=M^TS\left(M^{-1}\right)^T=M^{-1}SM.$$

Thus, the generalised LB method fulfils all of the requirements to simulate the quasi incompressible Navier-Stokes equations. The eigenvalues of the collision matrix corresponding to each eigenvector can be adjusted independently.

If the rows of M are orthogonal, then by definition

$$MM^T=Q,\quad MM^TQ^{-1}=I,$$

where Q is a diagonal matrix so the inverse is,

$$M^{-1}=M^TQ^{-1}.$$

Although the matrix inverse is easy to calculate, each time step does require two matrix vector multiplications.

2.3. Non-isotropic lattice

Using a rectangular lattice, the generalised LB method allows us to correctly set equilibrium moments from Eq. (4). Third order moments are unavoidably equal to the more complicated form shown in Eq. (10) since additional d^{sq} terms, equal to the grid size squared appear.

$$\sum c_{\mathbf{i}\alpha}c_{\mathbf{i}\beta}c_{\mathbf{i}\gamma}f^{eq}_{\mathbf{i}}=d^{sq}_{\alpha\beta}\sum c_{\mathbf{i}\beta}f^{eq}_{\mathbf{i}}$$
$$=d^{sq}_{\alpha\beta}\rho u_\beta \quad \text{if} \quad \alpha=\beta=\gamma.$$

The generalised LB method is able to correct the non-isotropic viscous term by applying a different relaxation rate to the diagonal terms of the viscous stress tensor, as demonstrated in Section 2.1.

The same method can be applied to other non-isotropic lattices such as the D3Q13 lattice [42]. It is also possible to correct these terms using a two relaxation time, quasi-equilibrium scheme [48,49]. The problem with non-isotropic viscosity has been recently discussed in a paper proposing a single relaxation time LB method using a rectangular grid [34] and a reply [50] highlighting the problem. More recently, Peng et. al. [38] have presented a Multiple Relaxation Time LB method that uses a non-isotropic two dimensional lattice. Compared to Peng. et. al., our method is more easily generalised to other lattices such as the three dimensional 27 speed lattice presented herein.

3. Moment basis

A set of orthogonal basis vectors and their equilibrium distributions must be defined in order to proceed using the moment based method. Linearly independent basis vectors are chosen and then the Gram-Schmidt process is used to make the set orthogonal. It is helpful if the basis vectors are closely related to the moments from Eq. (4) since these can then be set directly to their correct equilibrium values. In some cases, moments may be linearly dependent to others and hence cannot be used.

It is important to choose a set that allows the independent adjustment of each of the second order moments for use with a rectangular grid. Previously used orthogonal basis sets for the D2Q9, D2Q9 rectangular, D3Q15, D3Q13 and D3Q19 lattices [33,41,42,51] do not have this property. In these works, the authors selected the basis vectors based on physical quantities such as energy.

The basis vectors we have developed for the D2Q9 lattice are listed below with powers representing element by element operations and $c^{\,0}$ representing a vector of ones.

$$\psi_0=c^0,$$
$$\psi_1=c_x,$$
$$\psi_2=c_y,$$
$$\psi_3=3c_x^2-2\Delta x^2c^0,$$
$$\psi_4=3c_y^2-2\Delta y^2c^0,$$
$$\psi_5=c_xc_y,$$
$$\psi_6=3c_xc_y^2-2\Delta y^2c_x,$$
$$\psi_7=3c_yc_x^2-2\Delta x^2c_y,$$
$$\psi_8=9c_x^2c_y^2-6\Delta x^2c_y^2-6\Delta y^2c_x^2+4\Delta x^2\Delta y^2.$$

The basis vectors for the D3Q27 lattice are;

$$\psi_0=c^0,$$
$$\psi_1=c_x,$$
$$\psi_2=c_y,$$
$$\psi_3=c_z,$$
$$\psi_4=3c_x^2-2\Delta x^2c^0,$$
$$\psi_5=3c_y^2-2\Delta y^2c^0,$$
$$\psi_6=3c_z^2-2\Delta z^2c^0,$$
$$\psi_7=c_xc_y,$$
$$\psi_8=c_xc_z,$$
$$\psi_9=c_yc_z,$$
$$\psi_{10}=3c_xc_y^2-2\Delta y^2c_x,$$
$$\psi_{11}=3c_xc_z^2-2\Delta z^2c_x,$$
$$\psi_{12}=3c_yc_x^2-2\Delta x^2c_y,$$
$$\psi_{13}=3c_yc_z^2-2\Delta z^2c_y,$$
$$\psi_{14}=3c_zc_x^2-2\Delta x^2c_z,$$
$$\psi_{15}=3c_zc_y^2-2\Delta y^2c_z,$$

Table 1
Moment basis matrix M for the D2Q9 lattice. Each row is multiplied by the factor in the rightmost column.

1	1	1	1	1	1	1	1	1	1
0	1	−1	0	0	1	−1	−1	1	Δx
0	0	0	1	−1	1	−1	1	−1	Δy
−2	1	1	−2	−2	1	1	1	1	Δx^2
−2	−2	−2	1	1	1	1	1	1	Δy^2
0	0	0	0	0	1	1	−1	−1	$\Delta x\Delta y$
0	−2	2	0	0	1	−1	−1	1	$\Delta x\Delta y^2$
0	0	0	−2	2	1	−1	1	−1	$\Delta x^2\Delta y$
4	−2	−2	−2	−2	1	1	1	1	$\Delta x^2\Delta y^2$

$$
\begin{aligned}
\psi_{16} &= c_x c_y c_z,\\
\psi_{17} &= 9c_x^2c_y^2 - 6\Delta x^2c_y^2 - 6\Delta y^2c_x^2 + 4\Delta x^2\Delta y^2, \qquad \psi_{20} = 9c_y^2c_yc_z - 6\Delta x^2c_yc_z,\\
\psi_{18} &= 9c_x^2c_z^2 - 6\Delta x^2c_z^2 - 6\Delta z^2c_x^2 + 4\Delta x^2\Delta z^2, \qquad \psi_{21} = 9c_y^2c_xc_z - 6\Delta y^2c_xc_z,\\
\psi_{19} &= 9c_y^2c_z^2 - 6\Delta y^2c_z^2 - 6\Delta z^2c_y^2 + 4\Delta y^2\Delta z^2, \qquad \psi_{22} = 9c_z^2c_xc_y - 6\Delta z^2c_xc_y,\\
\psi_{23} &= 9c_x^2c_y^2c_z - 6\Delta x^2c_y^2c_z - 6\Delta y^2c_x^2c_z + 4\Delta x^2\Delta y^2c_z,\\
\psi_{24} &= 9c_x^2c_z^2c_y - 6\Delta x^2c_z^2c_y - 6\Delta z^2c_x^2c_y + 4\Delta x^2\Delta z^2c_y,\\
\psi_{25} &= 9c_y^2c_z^2c_x - 6\Delta y^2c_z^2c_x - 6\Delta z^2c_y^2c_x + 4\Delta y^2\Delta z^2c_x,\\
\psi_{26} &= 27c_x^2c_y^2c_z^2 - 8\Delta x^2\Delta y^2\Delta z^2c^0 - 18(\Delta x^2c_y^2c_z^2 + \Delta y^2c_x^2c_z^2 + \Delta z^2c_x^2c_y^2)\\
&\quad +12(\Delta x^2\Delta y^2c_z^2 + \Delta x^2\Delta z^2c_y^2 + \Delta y^2\Delta z^2c_x^2).
\end{aligned}
$$

The numerical forms of the resulting matrix M for the D2Q9 and D3Q27 lattice are shown in Tables 1 and 2.

The equilibrium moments up to third order in c_α are set directly to correct values, however we also need to define behaviour for higher order moments that appear in the orthogonal set. We make the following choices in order to replicate the properties of the single relaxation time model.

$$
\begin{aligned}
\sum c_x^2c_y^2f^{eq} &= \gamma_2\rho + \gamma_3\rho\left(u_x^2+u_y^2\right),\\
\sum c_x^2c_yc_zf^{eq} &= \gamma_4\rho u_yu_z,\\
\sum c_x^2c_y^2c_zf^{eq} &= \gamma_5\rho u_z,\\
\sum c_x^2c_y^2c_z^2f^{eq} &= \gamma_6\rho + \gamma_7\rho\left(u_x^2+u_y^2+u_z^2\right).
\end{aligned}
$$

The resulting equilibrium moments for the D2Q9 lattice are;

$$
\begin{aligned}
m_0^{eq} &= \rho, & m_6^{eq} &= \rho u_x\left(3c_s^2 - 2\Delta y^2\right),\\
m_1^{eq} &= \rho u_x, & m_7^{eq} &= \rho u_y\left(3c_s^2 - 2\Delta x^2\right),\\
m_2^{eq} &= \rho u_y,\\
m_3^{eq} &= \rho\left(3c_s^2 - 2\Delta x^2\right) + 3\rho u_xu_x,\\
m_4^{eq} &= \rho\left(3c_s^2 - 2\Delta y^2\right) + 3\rho u_yu_y,\\
m_5^{eq} &= \rho u_xu_y,\\
m_8^{eq} &= \rho\left(9\gamma_2 - 6c_s^2\left(\Delta x^2+\Delta y^2\right) + 4\Delta x^2\Delta y^2\right)\\
&\quad +\rho u_xu_x\left(9\gamma_3 - 6\Delta y^2\right) + \rho u_yu_y\left(9\gamma_3 - 6\Delta x^2\right).
\end{aligned}
$$

While the equilibrium moments for the D3Q27 lattice are;

$$
\begin{aligned}
m_0^{eq} &= \rho, & m_7^{eq} &= \rho u_xu_y,\\
m_1^{eq} &= \rho u_x, & m_8^{eq} &= \rho u_xu_z,\\
m_2^{eq} &= \rho u_y, & m_9^{eq} &= \rho u_yu_z,\\
m_3^{eq} &= \rho u_z, & m_{10}^{eq} &= \rho u_x(3c_s^2 - 2\Delta y^2),\\
m_4^{eq} &= \rho(3c_s^2 - 2\Delta x^2) + 3\rho u_xu_x & m_{11}^{eq} &= \rho u_x(3c_s^2 - 2\Delta z^2),\\
m_5^{eq} &= \rho(3c_s^2 - 2\Delta y^2) + 3\rho u_yu_y & m_{12}^{eq} &= \rho u_y(3c_s^2 - 2\Delta x^2),\\
m_6^{eq} &= \rho(3c_s^2 - 2\Delta z^2) + 3\rho u_zu_z & m_{13}^{eq} &= \rho u_y(3c_s^2 - 2\Delta z^2),\\
m_{14}^{eq} &= \rho u_z(3c_s^2 - 2\Delta x^2),\\
m_{15}^{eq} &= \rho u_z(3c_s^2 - 2\Delta y^2),
\end{aligned}
$$

$$
\begin{aligned}
m_{16}^{eq} &= 0,\\
m_{17}^{eq} &= \rho(9\gamma_2 - 6c_s^2(\Delta x^2+\Delta y^2) + 4\Delta x^2\Delta y^2)\\
&\quad +\rho u_xu_x(9\gamma_3 - 6\Delta dy^2) + \rho u_yu_y(9\gamma_3 - 6\Delta dx^2),\\
m_{18}^{eq} &= \rho(9\gamma_2 - 6c_s^2(\Delta x^2+\Delta z^2) + 4\Delta x^2\Delta z^2)\\
&\quad +\rho u_xu_x(9\gamma_3 - 6\Delta z^2) + \rho u_zu_z(9\gamma_3 - 6\Delta x^2),\\
m_{19}^{eq} &= \rho(9\gamma_2 - 6c_s^2(\Delta y^2+\Delta z^2) + 4\Delta y^2\Delta z^2)\\
&\quad +\rho u_yu_y(9\gamma_3 - 6\Delta z^2) + \rho u_zu_z(9\gamma_3 - 6\Delta y^2),\\
m_{20}^{eq} &= \rho u_yu_z(9\gamma_4 - 6\Delta x^2), \qquad m_{23}^{eq} = \rho u_z(9\gamma_5 - 6c_s^2(\Delta x^2+\Delta y^2)\\
&\qquad\qquad +4\Delta x^2\Delta y^2),\\
m_{21}^{eq} &= \rho u_xu_z(9\gamma_4 - 6\Delta y^2), \qquad m_{24}^{eq} = \rho u_y(9\gamma_5 - 6c_s^2(\Delta x^2+\Delta z^2)\\
&\qquad\qquad +4\Delta x^2\Delta z^2),\\
m_{22}^{eq} &= \rho u_xu_y(9\gamma_4 - 6\Delta z^2), \qquad m_{25}^{eq} = \rho u_x(9\gamma_5 - 6c_s^2(\Delta y^2+\Delta z^2)\\
&\qquad\qquad +4\Delta y^2\Delta z^2),\\
m_{26}^{eq} &= \rho\big[27\gamma_6 - 18\gamma_2(\Delta x^2+\Delta y^2+\Delta z^2) - 8\Delta x^2\Delta y^2\Delta z^2\\
&\quad +12c_s^2(\Delta x^2\Delta y^2 + \Delta x^2\Delta z^2 + \Delta y^2\Delta z^2)\big]\\
&\quad +\rho u_xu_x(27\gamma_7 - 18\gamma_3(\Delta y^2+\Delta z^2) + 12\Delta y^2\Delta z^2)\\
&\quad +\rho u_yu_y(27\gamma_7 - 18\gamma_3(\Delta x^2+\Delta z^2) + 12\Delta x^2\Delta z^2)\\
&\quad +\rho u_zu_z(27\gamma_7 - 18\gamma_3(\Delta x^2+\Delta y^2) + 12\Delta x^2\Delta y^2).
\end{aligned}
$$

In order to match equilibrium moments of the single relaxation time D2Q9 and D3Q27 lattices, the constants should take the following values;

$$
\begin{aligned}
c_s^2 &= \frac{h^2}{3}, \quad \gamma_2 = \frac{h^4}{9}, \quad \gamma_3 = \frac{h^2}{3},\\
\gamma_4 &= \frac{h^2}{3}, \quad \gamma_5 = \frac{h^4}{9}, \quad \gamma_6 = \frac{h^6}{27}, \quad \gamma_7 = \frac{h^4}{9}.
\end{aligned} \tag{16}
$$

The constant h is a characteristic grid size which should be equal to Δx for an isotropic grid and may be adjusted for a stretched grid. We have set $h = 1$ for all experiments.

4. Unsuitable lattices

As shown, it is possible to construct orthogonal basis vectors using the D2Q9 and D3Q27 lattices so that the eigenvalues for each of the square factors $c_{i\alpha}c_{i\beta}$ can be adjusted independently. Basis vectors involving multiple second order moments are problematic since they result in additional terms in the multi-scale expansion under some circumstances. Existing basis sets for the D2Q9, D2Q9 rectangular, D3Q15, D3Q13 and D3Q19 lattices [33,41,42,51] all feature such terms.

The multiplication of any of the vectors $c_\alpha c_\beta$ by A^{-1} must be equivalent to multiplication by some scalar, however if the vector under consideration is actually a linear combination of other eigenvectors, for example,

$$c_xc_x = E\psi_1 + F\psi_2,$$

where,

$$
\begin{aligned}
\psi_1 &= Ac_xc_x + Bc_yc_y,\\
\psi_2 &= Cc_xc_x + Dc_yc_y,
\end{aligned}
$$

then multiplication of c_xc_x by A^{-1} gives,

$$A^{-1}c_xc_x = E\lambda_1^{-1}\psi_1 + F\lambda_2^{-1}\psi_2.$$

Now if $\lambda_1 \neq \lambda_2$, there will be an additional factor of c_yc_y. The additional terms are not captured in the theoretical derivation and we would expect them to cause reduced accuracy. Factors proportional to c^0 are allowed to be combined with second order vectors since

Table 2
Moment basis matrix M for the D3Q27 lattice. Each row is multiplied by the factor in the rightmost column.

1	1	1	1	1	1	1	1	1	1	1	1	1	1	1	1	1	1	1	1	1	1	1	1	1	1	1	1
0	1	−1	0	0	0	0	1	−1	−1	1	1	−1	−1	1	0	0	0	0	1	−1	1	−1	1	−1	−1	1	Δx
0	0	0	1	−1	0	0	1	−1	1	−1	0	0	0	0	1	−1	−1	1	1	−1	1	−1	−1	1	1	−1	Δy
0	0	0	0	0	1	−1	0	0	0	0	1	−1	1	−1	1	−1	1	−1	1	−1	−1	1	1	−1	1	−1	Δz
−2	1	1	−2	−2	−2	−2	1	1	1	1	1	1	1	1	−2	−2	−2	−2	1	1	1	1	1	1	1	1	Δx^2
−2	−2	−2	1	1	−2	−2	1	1	1	1	−2	−2	−2	−2	1	1	1	1	1	1	1	1	1	1	1	1	Δy^2
−2	−2	−2	−2	−2	1	1	−2	−2	−2	−2	1	1	1	1	1	1	1	1	1	1	1	1	1	1	1	1	Δz^2
0	0	0	0	0	0	0	1	1	−1	−1	0	0	0	0	0	0	0	0	1	1	1	1	−1	−1	−1	−1	$\Delta x\Delta y$
0	0	0	0	0	0	0	0	0	0	0	1	1	−1	−1	0	0	0	0	1	1	−1	−1	1	1	−1	−1	$\Delta x\Delta z$
0	0	0	0	0	0	0	0	0	0	0	0	0	0	0	1	1	−1	−1	1	1	−1	−1	−1	−1	1	1	$\Delta y\Delta z$
0	−2	2	0	0	0	0	1	−1	−1	1	−2	2	2	−2	0	0	0	0	1	−1	1	−1	1	−1	−1	1	$\Delta x\Delta y^2$
0	−2	2	0	0	0	0	−2	2	2	−2	1	−1	−1	1	0	0	0	0	1	−1	1	−1	1	−1	−1	1	$\Delta x\Delta z^2$
0	0	0	−2	2	0	0	1	−1	1	−1	0	0	0	0	−2	2	2	−2	1	−1	1	−1	−1	1	1	−1	$\Delta y\Delta x^2$
0	0	0	−2	2	0	0	−2	2	−2	2	0	0	0	0	1	−1	−1	1	1	−1	1	−1	−1	1	1	−1	$\Delta y\Delta z^2$
0	0	0	0	0	−2	2	0	0	0	0	1	−1	1	−1	−2	2	−2	2	1	−1	−1	1	1	−1	1	−1	$\Delta z\Delta x^2$
0	0	0	0	0	−2	2	0	0	0	0	−2	2	−2	2	1	−1	1	−1	1	−1	−1	1	1	−1	1	−1	$\Delta z\Delta y^2$
0	0	0	0	0	0	0	0	0	0	0	0	0	0	0	0	0	0	0	1	−1	−1	1	−1	1	−1	1	$\Delta z\Delta y\Delta z$
4	−2	−2	−2	−2	4	4	1	1	1	1	−2	−2	−2	−2	−2	−2	−2	−2	1	1	1	1	1	1	1	1	$\Delta x^2\Delta y^2$
4	−2	−2	4	4	−2	−2	−2	−2	−2	−2	1	1	1	1	−2	−2	−2	−2	1	1	1	1	1	1	1	1	$\Delta x^2\Delta z^2$
4	4	4	−2	−2	−2	−2	−2	−2	−2	−2	−2	−2	−2	−2	1	1	1	1	1	1	1	1	1	1	1	1	$\Delta y^2\Delta z^2$
0	0	0	0	0	0	0	0	0	0	0	0	0	0	0	−6	−6	6	6	3	3	−3	−3	−3	−3	3	3	$\Delta x^2\Delta y\Delta z$
0	0	0	0	0	0	0	0	0	0	0	−6	−6	6	6	0	0	0	0	3	3	−3	−3	3	3	−3	−3	$\Delta y^2\Delta x\Delta z$
0	0	0	0	0	0	0	−6	−6	6	6	0	0	0	0	0	0	0	0	3	3	3	3	−3	−3	−3	−3	$\Delta z^2\Delta x\Delta y$
0	0	0	0	0	4	−4	0	0	0	0	−2	2	−2	2	−2	2	−2	2	1	−1	−1	1	1	−1	1	−1	$\Delta x^2\Delta y^2\Delta z$
0	0	0	4	−4	0	0	−2	2	−2	2	0	0	0	0	−2	2	2	−2	1	−1	1	−1	−1	1	1	−1	$\Delta x^2\Delta z^2\Delta y$
0	4	−4	0	0	0	0	−2	2	2	−2	−2	2	2	−2	0	0	0	0	1	−1	1	−1	1	−1	−1	1	$\Delta y^2\Delta z^2\Delta x$
−8	4	4	4	4	4	4	−2	−2	−2	−2	−2	−2	−2	−2	−2	−2	−2	−2	1	1	1	1	1	1	1	1	$\Delta x^2\Delta y^2\Delta z^2$

Table 3
Dot products relevant to finding orthogonal vectors for various lattices.

Lattice	$c^0 \cdot c^0$	$c_x^2 \cdot c_x^2$	$c_y^2 \cdot c_y^2$	$c_x^2 \cdot c_y^2$
D3Q15	15	10	10	8
D3Q19	19	10	10	4

any additional terms generated drop out,

$$\sum_{i=0}^{q} c_i^0 f_i^{(1)} = \sum_{i=0}^{q} f_i^{(1)} = 0.$$

It is impossible to form the correct basis vectors using the D3Q19 and D3Q15 lattices. We find that there is no way to have $c_x c_x$ orthogonal to $c_y c_y$ and similarly for other combinations. We wish to construct basis vectors of the form,

$$\psi_0 = c^0,$$
$$\psi_1 = c_x c_x + A c^0,$$
$$\psi_2 = c_y c_y + B c^0.$$

The orthogonal requirements lead to the constraints;

D3Q15:

$$\psi_1 \cdot \psi_0 = 0, \Rightarrow 10 + 15A = 0.$$
$$\psi_2 \cdot \psi_0 = 0, \Rightarrow 10 + 15B = 0.$$
$$\psi_1 \cdot \psi_2 = 0, \Rightarrow 8 + 10A + 10B + 15AB = 0.$$

D3Q19:

$$\psi_1 \cdot \psi_0 = 0, \Rightarrow 10 + 19A = 0.$$
$$\psi_2 \cdot \psi_0 = 0, \Rightarrow 10 + 19B = 0.$$
$$\psi_1 \cdot \psi_2 = 0, \Rightarrow 4 + 10A + 10B + 19AB = 0.$$

The relevant dot products for the D3Q19 and D3Q15 lattice are listed in Table 3. If the first two constraints are met for each lattice, then the third cannot be.

D3Q15: $\psi_1 \cdot \psi_2 = 8 - 2\frac{100}{15} + \frac{100}{15} \neq 0.$

D3Q19: $\psi_1 \cdot \psi_2 = 4 - 2\frac{100}{19} + \frac{100}{19} \neq 0.$

5. Stability

There has been significant work on the stability of the LB method, beginning with linear perturbation analysis [41,52] and progressing to increasingly more complex techniques [53–56]. The stability properties of applications such as turbulent channel flow simulation are well predicted by linear perturbation analysis, in particular the flow is sensitive to a mean background velocity. In addition to analysing stability, linear perturbation analysis can also provide insight into physically meaningful properties of the scheme such as the relationship between viscosity and speed of sound and the wavelength of the perturbation, also known as a dispersion relation.

Each scheme with q velocity basis vectors also has q eigenmodes, each with a corresponding eigenvector. It is found that three physically meaningful modes are always present, two acoustic waves with opposite propagation velocities and one transverse shear wave. The rate of decay of these modes is related to the real component of the logarithm of the eigenvalue leading to a derived viscosity. Likewise, the wave speed is related to the complex angle and a speed of sound can be derived. These properties are shown for all eigenvalues of the 9 speed lattice in Fig. 2. Some eigenvalues are repeated leading to only 5 distinct lines.

The viscosity and speed of sound are calculated for each wavenumber and normalised by the zero wavenumber value which exactly corresponds to the value that is obtained from multi-scale expansion as shown in Fig. 3. These plots show curves for Δy ranging from half to one and a perturbation that varies along the y direction. When the perturbation was instead varied along the x direction with these same grid sizes, the dispersion relations did not change from the values obtained using a uniform grid, hence these null results are not shown for brevity. The zero wavenumber values do not change as the grid size is changed which confirms that the viscosity and speed of sound are correctly reproduced in agreement with the multi-scale expansion. The grid aspect ratios investigated herein do not show any deterioration in the dispersion relation compared to a uniform grid. The speed of sound disper-

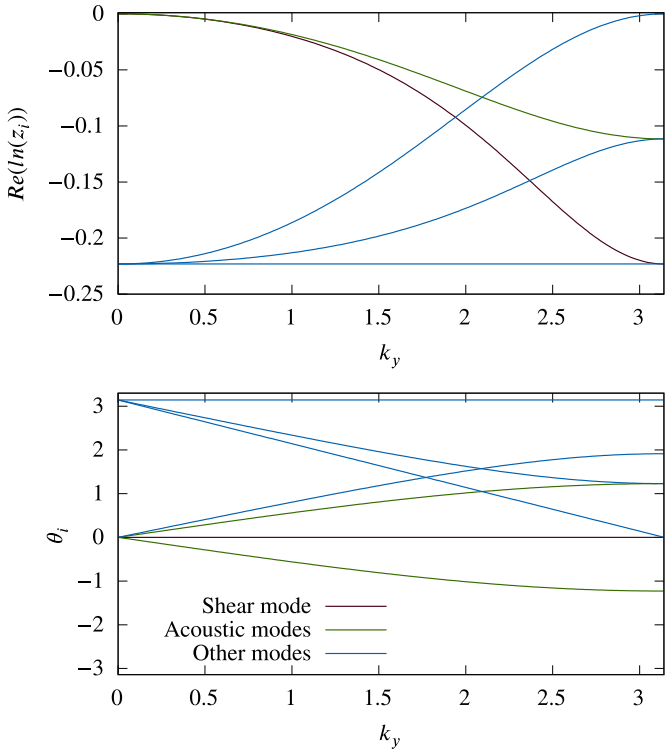

Fig. 2. Logarithm of eigenvalue magnitude (top) and eigenvalue complex angle (bottom).

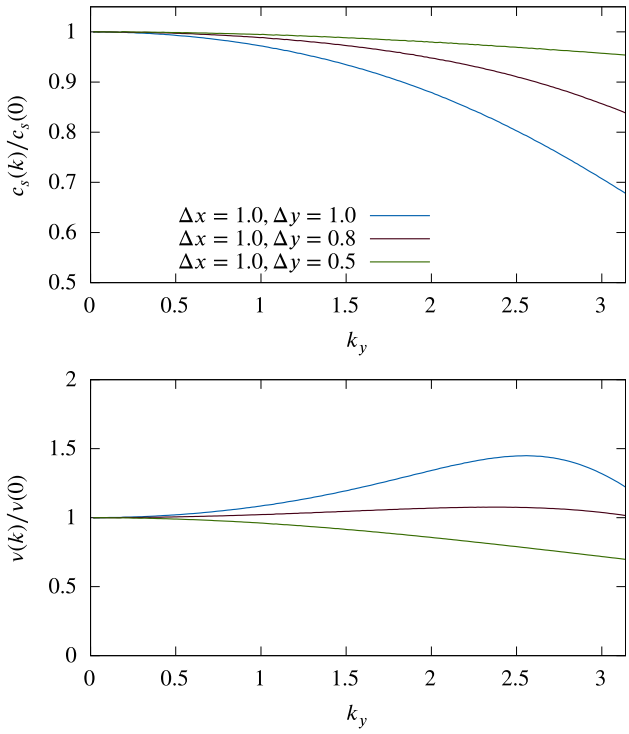

Fig. 3. Speed of sound and viscosity dispersion relations. Each quantity is plotted against wavenumber and normalised by zero wavenumber value.

sion relation improves as the grid is stretched while the viscosity dispersion relation changes sign from an increase to a decrease in viscosity at small wavenumbers as the grid is stretched. The most uniform viscosity dispersion relation was obtained when $\Delta y = 0.8$ was used.

Our stability analysis method is based on the technique set out by Lallemand and Luo [41], however we set a uniform background velocity always in the x direction and then look at all wave numbers of perturbation at all angles to this direction. This is in contrast to the original method that assumed the fastest growing mode was parallel to the flow and varied the direction of the flow and perturbation simultaneously. We have found that the fastest growing unstable wavenumber is not necessarily aligned with the flow direction and verified this by observing unstable simulation examples that show growing non-physical oscillations that tend not to be aligned with the flow direction.

We tested perturbations with a discrete range of wave numbers, evenly distributed between zero and π in three dimensions. Fig. 4 shows the maximum attainable velocity for a square grid with 32 and 16 wavelengths tested in each direction as well as a trial only testing integer wavelengths. The curves get increasingly smooth as the number of wave numbers tested increases. We have used 32 wave numbers in all subsequent tests in a trade off between computational effort and accuracy.

Figs. 5 and 6 show maximum velocity for a range of aspect ratios a when the grid is simultaneously stretched in the direction of the mean flow and in one perpendicular direction as shown in the inset. The results differ depending on whether the overall size is decreased as in Fig. 5 or increased as in Fig. 6. The stability for small aspect ratios is significantly better if the grid size is decreased. There appears to be an optimal grid size that varies with aspect ratio. Changing the grid size is equivalent to modifying the scaling factor h used in the equilibrium constants. There appears to be an optimal value for each aspect ratio that has not been calculated here.

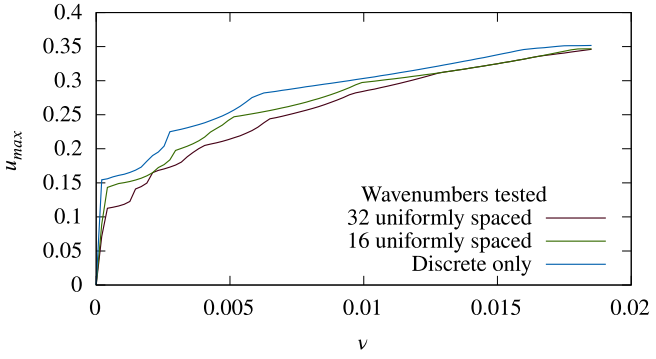

Fig. 4. Maximum attainable velocity vs viscosity. Perturbations with 32 and 16 uniformly spaced wave-numbers and perturbations with discrete wavelengths only tested in three dimensions using a square grid.

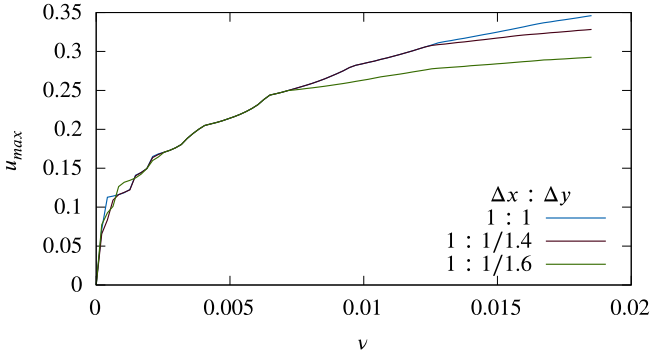

Fig. 5. Maximum attainable velocity vs viscosity for a range of aspect ratios, longest grid dimension aligned with velocity.

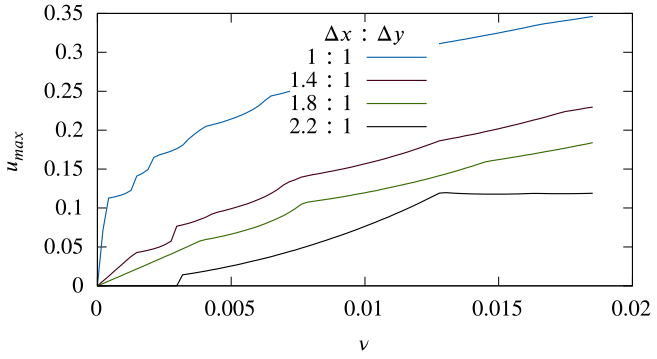

Fig. 6. Maximum attainable velocity vs viscosity for a range of aspect ratios, longest grid dimension aligned with velocity.

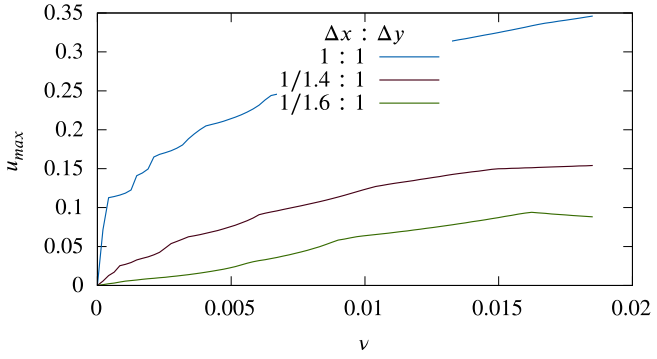

Fig. 7. Maximum attainable velocity vs viscosity for a range of aspect ratios, shortest grid dimension aligned with velocity.

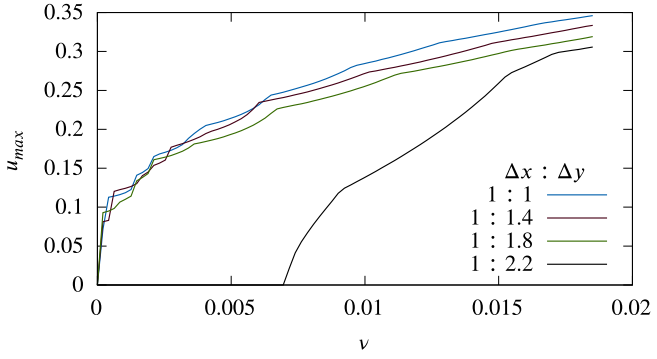

Fig. 8. Maximum attainable velocity vs viscosity for a range of aspect ratios, shortest grid dimension aligned with velocity.

The stability properties also depend on the direction of stretching. Figs. 7 and 8 show maximum velocity for a range of aspect ratios a when the grid is simultaneously stretched in two directions perpendicular to the mean flow as shown in the inset. This time the stability at moderate aspect ratios is better when the grid size is increased.

5.1. Chequerboard invariant

The D3Q27 and D3Q15 lattices support a conserved chequerboard invariant [40–42]. This mode may be harmless or may cause spurious oscillations depending on boundary and initial conditions. Qian [57] has shown the elimination of other undesired invariants for one dimensional simulations by using fractional propagation, that is, making the lattice spacing larger than the particle velocity by some factor and the Courant number for particle advection less than one.

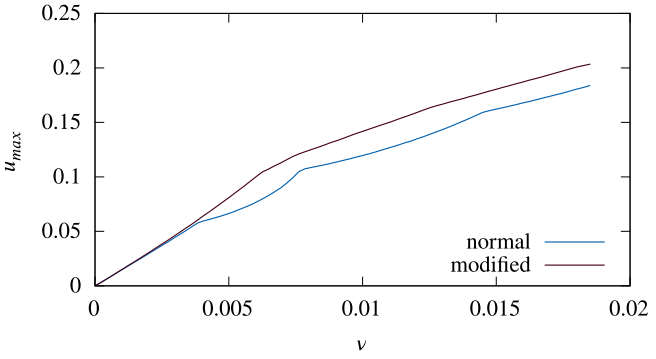

Fig. 9. Maximum attainable velocity vs viscosity for an aspect ratio of 1: 1.8, configuration shown in inset. Normal scheme compared to one where relaxation rates have been reduced by a factor of 0.9 for odd order moments.

We have previously used a smaller than unit Courant number successfully for this reason [46]. A Courant number of 0.9 has been used in all stability tests above as well as all numerical simulations. Our linear stability analysis and observations of unstable channel flow simulations support this hypothesis.

5.2. Stability improvements

The generalised LB method allows potential improvements to stability by independently adjusting the relaxation rate of non-hydrodynamic 'ghost' moments. Lallemand and Luo originally proposed keeping the relaxation rates fixed at their most stable values however later analysis by Dellar [43] showed that due to higher order coupling, the relaxation rates for these 'ghost' moments need to be scaled in proportion to the other relaxation rates in order to achieve convergence in the low Mach number limit. A related stabilization method for single relaxation time LB methods introduced by Latt and Chopard [55], keeps all non-hydrodynamic moments at zero.

We have experimented with reduced relaxation rates for non-hydrodynamic moments and have found the results to be less effective when applied to the D3Q27 lattice than initial experiments with the D2Q9 lattice. The first experiment was to simply reduce all unconstrained relaxation rates by some factor and this failed to increase the maximum attainable velocity. Next we modified groups of eigenvalues, treating the third, fourth, fifth and sixth order moments separately, and found that high relaxation rate stability could be improved by decreasing the relaxation rate for the odd moments only. Fig. 9 shows results for an aspect ratio of 1: 1.8 comparing the normal scheme to one where odd order non-hydrodynamic moments use a relaxation rate multiplied by a factor of 0.9 compared to the base relaxation rate. The modified scheme has a slightly improved maximum velocity over a range of relaxation rates. This modification was not used in subsequent simulations because the improvements at this stage require further investigation.

Previous work on the rectangular LB method in two dimensions [33] reported improved stability and accuracy by changing the speed of sound as a function of aspect ratio. We have not tested other speeds of sound or any other equilibrium parameters. As mentioned in the previous sections, the overall grid size or equivalently the scaling factor h could also be adjusted.

6. Numerical results

The new non-isotropic scheme proposed in this work has been tested by performing numerical simulations of Taylor-Green vortex flow and turbulent channel flow in order to verify its expected

theoretical properties. Laminar channel flow testing was also performed however the results for this simple flow were identical to all significant figures printed when the grid was stretched along the stream-wise direction. Since laminar channel flow only has two terms in the Navier-Stokes equations that are non-zero, that is the span-wise velocity gradient and force term, it does not represent a challenging test of accuracy for the solver, thus the results are not included. In cases where the flow is dominated by gradients in only one direction such as boundary layers, the present scheme with the grid size increased along the stream-wise direction is expected to yield reduced computational effort, as demonstrated by the turbulent channel flow simulation results in Section 6.2.

All simulations were performed using a lattice Boltzmann based code that we have previously developed [2]. The code is written mostly in the C programming language and used Nvidia's CUDA extensions in order to run on graphics processing units (GPUs). Additional details relevant to the numerical implementation regarding initialization, boundary conditions and forcing follow.

Periodic boundary conditions do not require any additional analysis when applied to the LB method however boundary conditions based on hydrodynamic variables such as the non-slip boundary used in the channel flow simulation are non trivial to implement. The most simple wall boundary condition is the bounce-back type where particle populations impacting the wall simply bounce back to their source site during the streaming step. The order of accuracy of the scheme near such walls may be reduced to first order depending on the relaxation factor. We have used the bounce-back boundary condition since we are more interested in comparing the relative accuracy of the normal and modified schemes rather than obtaining the most accurate solution possible.

The initialization of lattice Boltzmann methods has also been a subject of active research [58–60]. The initial density field must correctly describe the pressure field corresponding to the Navier-Stokes equations otherwise non physical pressure fluctuations will be introduced. Also, the non-equilibrium moments must be initialized to correct values in order for the initial particle population to correctly approximate hydrodynamic behaviour. We have used a finite difference approximation for non-equilibrium moments and the analytical pressure field to initialize the Taylor-Green vortex simulation. The channel flow was simply initialised to equilibrium values for the prescribed velocity field under the assumption that initial errors would decay well before the flow reached a statistically stationary state and measurements began.

The channel flow simulation is driven by a body force h_α equivalent to a pressure gradient and implemented by adding an additional term F_i to the evolution equation,

$$F_i = W_i \frac{1}{c_s^2} c_{i\alpha} h_\alpha \tag{17}$$

Here W_i are lattice weights used by the single relaxation time method. This simple treatment of the body force, in contrast to other more accurate methods analysed by Guo et al. [61], is acceptable since the body force in this case is constant in both time and space.

6.1. Asymptotic convergence

We tested the asymptotic convergence of the present scheme by simulating Taylor-Green (TG) vortex flow and analysing the behaviour of the L2 norm of velocity error as the Mach number, Reynolds number and grid resolution were varied. The Taylor-Green vortex has an analytical solution that varies in two spatial dimensions and time,

$$u(x, y, t) = u_0 e^{-2k_0^2 \nu t} \cos(k_0 x) \sin(k_0 y),$$

Table 4
Domain configurations used for the simulation of Taylor-Green vortex flow.

n_x	n_y	Δ_x	Δ_y	Re
8, 11 and 16	8	1	1, 1.375 and 2	1 and 10
16, 22 and 32	16	1	1, 1.375 and 2	1 and 10
32, 45 and 64	32	1	1, 1.40625 and 2	1 and 10
64, 90 and 128	64	1	1, 1.40625 and 2	1 and 10
128, 181 and 256	128	1	1, 1.4140625 and 2	1 and 10
256, 362 and 512	256	1	1, 1.4140625 and 2	1 and 10

Table 5
Parameters used for the simulation of turbulent channel flow.

	n_x	Δx	n_y	Δy	n_z	Δz	N_{tot}
142	448	1	142	1	226	1	14 million
160 stretch	352	1	160	0.71429	178	1	10 million

$$v(x, y, t) = -u_0 e^{-2k_0^2 \nu t} \sin(k_0 x) \cos(k_0 y),$$
$$k_0 = 2\pi / l_0. \tag{18}$$

The analytical solution for pressure is,

$$P(x, y, t) = P_0 + \frac{u_0^2}{4} e^{-4k_0^2 \nu t} \cos(2k_0 x) \cos(2k_0 y). \tag{19}$$

Here l_0 is the length of the domain which is equal in the x and y directions.

$$l_0 = n_x \cdot \Delta x = n_y \cdot \Delta y.$$

We calculate the L2 error norm at a prescribed non-dimensional time,

$$t^* = 2k_0^2 \nu t$$

chosen so that the characteristic velocity had reduced by a factor of four,

$$e^{-t^*} = \frac{1}{4}, \quad t^* \sim 1.3863.$$

The problem is fully specified by the two non-dimensional parameters, the Reynolds number and the Mach number,

$$\mathrm{Re} = \frac{u_0 \cdot l_0}{\nu} \quad \text{and} \quad \mathrm{Ma} = \frac{u_0}{c_s}.$$

The other problem parameters ν and u_0 are calculated from the above. Simulations are performed over a range of parameters, with Reynolds numbers of 1 and 10 used, number of grid points varied between 8 and 512 and Mach number varied between 0.0015625 and 0.1 as listed in Table 4.

The numerical errors present during the simulation of TG vortex flow can be dominated by errors due to incorrect initialization of the flow field [60]. In order to minimise these errors, the density was initialized to the analytic solution for pressure and the second order non-equilibrium moments were initialized based on exact values based on the prescribed velocity.

Results shown in Fig. 10 illustrate Mach number convergence. When the Reynolds number is 1, all grid sizes and aspect ratios follow a similar trend. The L2 error norm decreases as the Mach number is reduced following a second order trend as expected based on multi-scale expansion. This error behaviour is generally consistent with other studies [21,62]. The results with an aspect ratio of 1.41 are slightly anomalous with error that is reduced compared to other results and an apparent order of accuracy slightly greater than two. When the Reynolds number is increased to 10 the uniform grid results exhibit the same behaviour again although at this Reynolds number, the stretched grid simulations reach a limit below which error fails to continue reducing. The error plateaus at this low Mach number error limit which occur at a Mach number around 0.00625 and depends on the grid resolution. The two grid

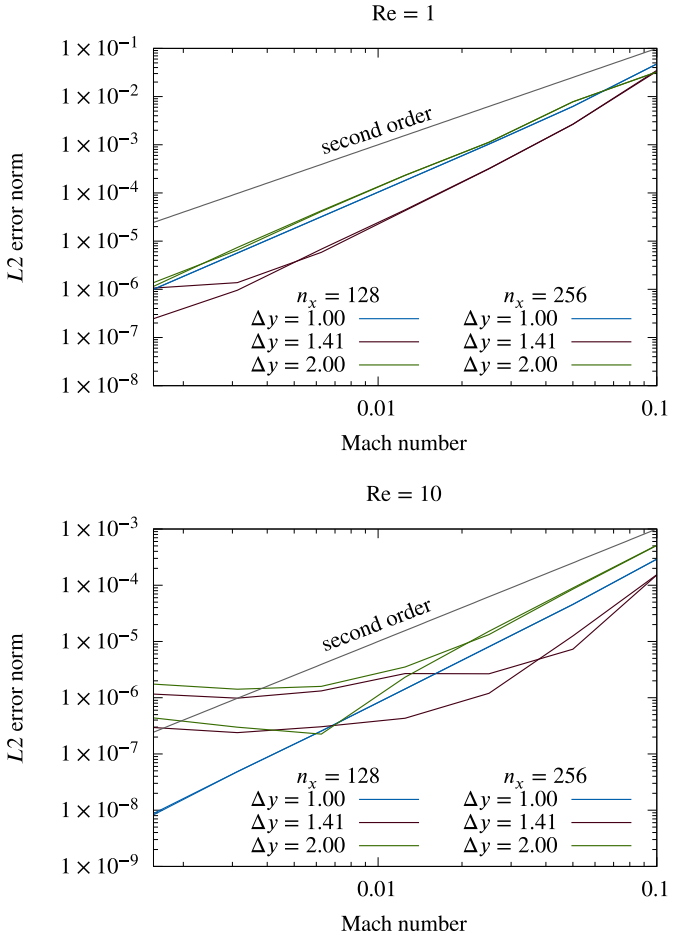

Fig. 10. L2 error norm of Taylor-Green vortex simulation at various Mach numbers, grid resolutions and aspect ratios. Measurements taken at non-dimensional time $t* = 1.3863$. Reynolds number 1 (top) and 10 (bottom).

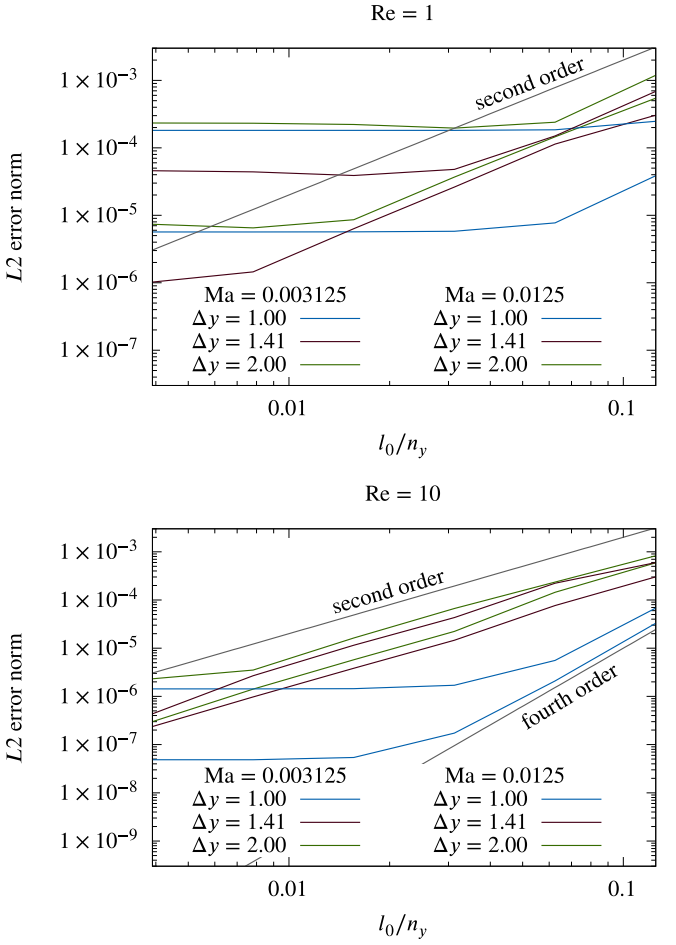

Fig. 11. L2 error norm of Taylor-Green vortex simulation at various Mach numbers, grid resolutions and aspect ratios. Measurements taken at non-dimensional time $t* = 1.3863$. Reynolds number 1 (top) and 10 (bottom).

resolutions (solid and dashed) are nearly overlapping in the Mach number range where the stretched grids demonstrate asymptotic convergence, while they diverge at smaller Mach numbers where the error plateaus, with more grid points decreasing the error indicating that grid errors are more dominant in that range. We conclude that the above results are consistent with asymptotic convergence that depends on both the Mach number and number of grid points - the grid needs to have sufficient points so that grid errors are negligible in order to demonstrate Mach number convergence and vice versa the Mach number needs to be sufficiently small to demonstrate grid convergence. This is further demonstrated by the grid convergence plots.

The L2 error norm is plotted against the inverse of the number of grid points as shown in Fig. 11 in order to investigate grid convergence. At a Reynolds number of 10 the stretched grid simulations follow a second order trend. Here the uniform grid simulations follow a fourth order trend before reaching a plateau where further increases in grid resolution do not reduce error. This indicates that Mach number errors have become dominant. At a Reynolds number of one all simulations reach a similar plateau. The smaller Mach number series (solid) continue further before reaching the plateau compared to the higher Mach number simulation (dashed).

The relationship between error, Mach number, Reynolds number and grid resolution is complicated. Second order asymptotic grid convergence is observed with continued reduction in error being limited by Mach number errors becoming dominant. Likewise second order asymptotic Mach number convergence is observed with continued reduction in error being limited by grid errors becoming dominant. These boundaries vary between uniform and stretched grids however the error behaviour is broadly consistent with the expected second order behaviour. Based on the fourth order grid convergence demonstrated for the uniform grid, it is possible that the simple trigonometric form of the solution leads to some cancellation of higher order error terms that will not occur in a more general case and that does not occur for the stretched grid. An analogous example occurs when a second order finite difference scheme is used to simulate the wave equation. If the accuracy is tested using a sinusoidal initial condition then fourth order results can be obtained leading to an improper conclusion regarding accuracy. This reasoning leads to the conclusion that the uniform grid results are unrepresentative while the stretched grid results are realistic. It is not possible to explain this based on the second order multi-scale expansion that is used to develop this lattice Boltzmann scheme.

We note that Peng et. al. [38] found orders of accuracy that varied significantly between 0.65 and 3.52 for their stretched grid lattice Boltzmann scheme. In practice, stretched grids are not intended to be used for flow fields such as the Taylor-Green vortex which have similar gradients in both directions so while the error behaviour is acceptable the advantage of the present scheme is for simulating wall bounded flows such as turbulent channel flow which follows.

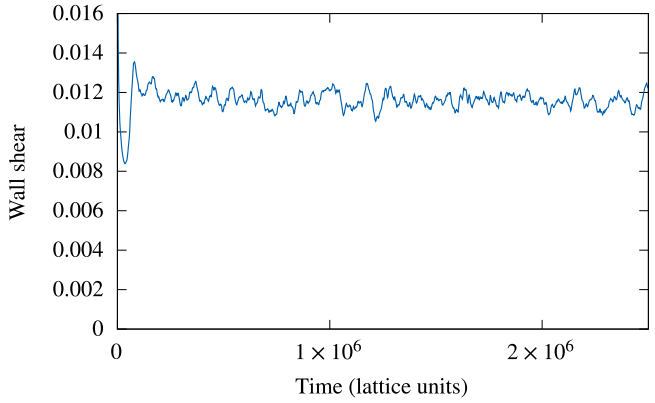

Fig. 12. Evolution of wall shear with time for LB simulation using rectangular grid.

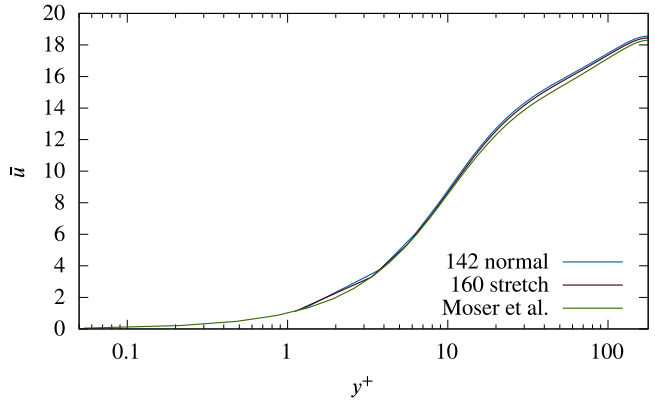

Fig. 13. Mean velocity, normalised by the friction velocity comparing lattice Boltzmann simulations to results of Moser et al. [44].

6.2. Turbulent channel flow

We further tested the present scheme by performing a direct numerical simulation of fully turbulent channel flow using a method similar to our previous work [2]. We compare the mean velocity and turbulent kinetic energy (TKE) profiles with results of Moser et al. [44].

The simulation was performed at a wall Reynolds number of 180,

$$Re_\tau = \frac{u_\tau \delta}{\nu} = 180.$$

Friction velocity is defined as,

$$u_\tau = \sqrt{\frac{\tau_w}{\rho}}$$

and the wall shear τ_w is related to the applied body force h, by a static balance of forces

$$h\delta = \tau_w = \mu \left.\frac{\partial u}{\partial y}\right|_{y=0}.$$

The non-dimensional height of the domain δ is 2 in the y direction. The stream-wise and span-wise domain size are 2π and π in the x and z directions respectively. We performed two simulations, first with a uniform grid and then with a stretched grid. The simulation with a stretched grid allowed the use of a higher resolution in the wall-normal direction while reducing the total number of nodes from 14 million to 10 million. A Mach number of 0.1 was used for both simulations. The flow was initialised to a one seventh power law mean velocity profile with a divergence free velocity perturbation superimposed in order to trigger the transition to turbulence. The simulation was then allowed to progress for 1000 eddy turnover times (roughly one million time steps)

$$t_{\text{eddy}} = \frac{\delta}{u_{\max}},$$

before beginning to sample statistics for a further 1500 turnover times in order to reach a statistically stationary result. Fig. 12 shows the evolution of wall shear over this time.

Fig. 13 shows the mean velocity profiles while Figs. 14 and 15 show turbulent kinetic energy profiles for the cases investigated. Results obtained using the LB method over-predict the TKE peaks and centerline mean velocity. The dominant errors in this simulation arise from insufficient resolution near the walls, the benchmark results of Moser et al. use a much finer grid resolution near the wall in order to capture the sharp gradients. The y^+ value for the node nearest to the wall in our simulation was 1.11 using a stretched grid and 1.25 using a uniform grid while the simulation

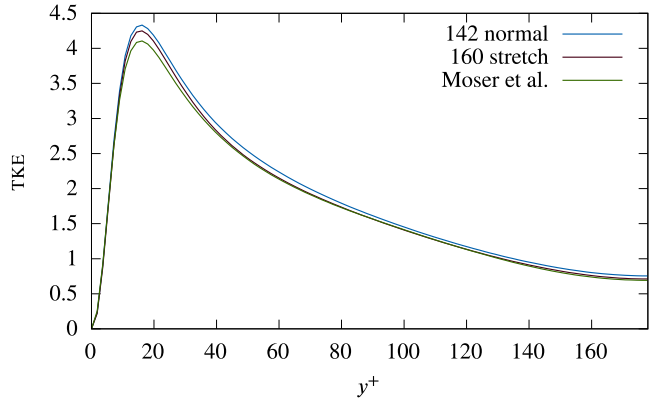

Fig. 14. Turbulent kinetic energy comparing lattice Boltzmann simulations to results of Moser et al. [44].

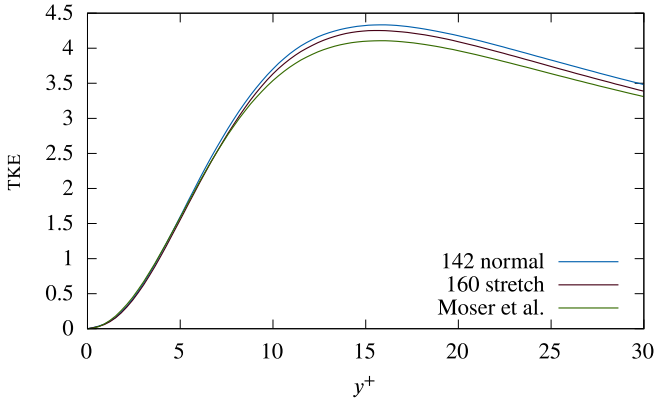

Fig. 15. Near wall turbulent kinetic energy comparing lattice Boltzmann simulations to results of Moser et al. [44].

of Moser et al. used grid refinement to place five nodes within this distance of the wall despite having fewer nodes overall in the wall normal direction. The simulation performed using a stretched grid achieves better agreement with the benchmark results despite using 40% fewer nodes with a corresponding decrease in simulation speed and memory usage. The increase in computational efficiency is partially offset by the necessary use of the D3Q27 lattice rather than the more commonly used D3Q19 or D3Q15 lattices.

7. Discussion and conclusions

We have presented a lattice Boltzmann scheme using a rectangular grid and non-isotropic lattices to simulate quasi-incompressible fluid dynamics in two and three dimensions. We have shown that the scheme correctly models Navier-Stokes behaviour according to a second order multi-scale expansion similarly to other LB methods.

The multi-scale expansion presented in this paper represents the non-isotropic part of the third order equilibrium moments in terms of a rank four Kronecker delta and offers new insights into the underlying dynamics compared to perturbation analysis used to deal with non-isotropic lattices in previous work [33,42]. This methodology is also more general with respect to lattices — Eq. (13) can be used to correctly adjust the eigenvalues of the collision matrix for a range of non-isotropic lattices including the rectangular D2Q9 and D3Q27 lattices and the square D3Q13 lattice. The orthogonal basis vectors presented in this paper improve accuracy compared to previous work using a rectangular lattice [33] and we have shown that it is not possible to construct an orthogonal basis with similar properties for the commonly used D3Q15 and D3Q19 lattices.

Linear perturbation analysis reveals an instability that is sensitive to the mean background velocity, similarly to standard LB methods. The maximum background velocity is reduced as the grid is stretched in the direction of the flow. In contrast to other linear perturbation studies [41], we have found that the fastest growing unstable mode is at an angle to the mean flow. We attempted to improve stability by reducing the relaxation rates for non-hydrodynamic moments however improvements were not effective. We have also investigated the dispersion relations between speed of sound and viscosity and wave number finding that the stretched grid does not introduce any new errors and produces consistent results.

The asymptotic error behaviour of the present scheme using a rectangular grid with various aspect ratios was tested by simulating Taylor-Green vortex flow and was found to match the expected order of accuracy of the LB method, that is second order in Mach number and number of grid points. In some cases there were differences in results between uniform and stretched grids however these differences are nevertheless consistent with the aforementioned order of accuracy. Laminar channel flow simulations using stretched and uniform grids produced identical results due to the simplicity of the test case. These results were not included, instead a more challenging case, turbulent channel flow was included.

The present scheme using a stretched grid with an increased wall-normal resolution was used to successfully simulate turbulent channel flow to a higher accuracy than the standard LB method and with a reduced computational effort. The stretched grid simulation used 40% fewer nodes than the normal method, significantly decreasing simulation time while simultaneously improving accuracy. The successful simulation further verifies stability and accuracy of the method presented in this work and indicates its potential application to other turbulent three dimensional flows.

The scheme has been shown to be useful despite additional stability and accuracy concerns that can accompany non-uniform grid LB methods. It is expected that further analysis of higher order errors could yield improvements both stability and accuracy.

Declaration of Competing Interest

The authors declare that they do not have any financial or non-financial conflict of interests.

CRediT authorship contribution statement

Vanja Zecevic: Conceptualization, Methodology, Software, Validation, Formal analysis, Investigation, Resources, Data curation, Writing - original draft, Writing - review & editing, Project administration. **Michael P. Kirkpatrick:** Writing - review & editing, Supervision, Funding acquisition. **Steven W. Armfield:** Writing - review & editing, Supervision, Funding acquisition.

Acknowledgment

This work has been supported by Australian Research Council Discovery Grant dp150100912.

Appendix A. Multi scale expansion

This appendix demonstrates a multi-scale expansion of the lattice Boltzmann method with a linear collision operator. The resulting method approaches the incompressible Navier-Stokes equations as the compressibility errors, proportional to the Mach number squared, approach zero. Further discussion regarding obtaining the correct form for viscous terms when using a stretched grid is presented in Section 2.

Time advancement of the particle populations is calculated using first order upwind streaming and an upwind collision operator,

$$f_{\boldsymbol{i}}(x_\alpha + \Delta x_\alpha, t + \Delta t) = (1 - Cr) f_{\boldsymbol{i}}(x_\alpha + \Delta x_\alpha, t) + Cr f_{\boldsymbol{i}}(x_\alpha, t) + \Delta t \Omega_{\boldsymbol{i}}(x_\alpha, t), \tag{A.1}$$

where Cr is the Courant number for particle advection,

$$Cr = \frac{||c_{\boldsymbol{i}\alpha}||\Delta t}{||\Delta x_\alpha||}$$

and Ω is the linearised collision operator,

$$\Omega_{\boldsymbol{i}}(x_\alpha, t) = \sum_{\boldsymbol{j}=0}^{q} A_{\boldsymbol{ij}} \left(f_{\boldsymbol{j}}(x_\alpha, t) - f_{\boldsymbol{j}}^{eq}(x_\alpha, t) \right). \tag{A.2}$$

The particle population is decomposed into equilibrium and non-equilibrium $f_{\boldsymbol{i}}^{neq}$ components,

$$f_{\boldsymbol{i}} = f_{\boldsymbol{i}}^{eq} + f_{\boldsymbol{i}}^{neq}. \tag{A.3}$$

The non-equilibrium component is expanded in the small parameter ϵ which is taken to be the Knudsen number,

$$f_{\boldsymbol{i}}^{neq} = \epsilon f_{\boldsymbol{i}}^{(1)} + \epsilon^2 f_{\boldsymbol{i}}^{(2)} + \mathcal{O}\left(\epsilon^3\right).$$

Derivatives are also redefined using the multi-scale expansion as,

$$\partial_t = \epsilon \partial_{t_1} + \epsilon^2 \partial_{t_2} \text{ and } \partial_\alpha = \epsilon \partial_{\alpha_1}. \tag{A.4}$$

Density and momentum are conserved moments of the particle distributions,

$$\sum_{\boldsymbol{i}=0}^{q} f_{\boldsymbol{i}} = \sum_{\boldsymbol{i}=0}^{q} f_{\boldsymbol{i}}^{eq} = \rho, \tag{A.5a}$$

$$\sum_{\boldsymbol{i}=0}^{q} c_{\boldsymbol{i}\alpha} f_{\boldsymbol{i}} = \sum_{\boldsymbol{i}=0}^{q} c_{\boldsymbol{i}\alpha} f_{\boldsymbol{i}}^{eq} = \rho u_\alpha. \tag{A.5b}$$

It follows that,

$$\sum_{\boldsymbol{i}=0}^{q} f_{\boldsymbol{i}}^{neq} = 0 \text{ and } \sum_{\boldsymbol{i}=0}^{q} c_{\boldsymbol{i}\alpha} f_{\boldsymbol{i}}^{neq} = 0. \tag{A.6}$$

The collision operator becomes,

$$\Omega_{\boldsymbol{i}}(x_\alpha, t) = \epsilon \sum_{\boldsymbol{j}=0}^{q} A_{\boldsymbol{ij}} f_{\boldsymbol{j}}^{neq}(x_\alpha, t). \tag{A.7}$$

Thus the collision operator does not change the momentum or mass,

$$\sum_{i=0}^{q} \Omega_i = 0 \text{ and } \sum_{i=0}^{q} c_{i\alpha}\Omega_i = 0. \tag{A.8}$$

In order to correctly model compressible flow, energy should also be a conserved moment however in the common quasi-incompressible approach energy is not conserved. As a result, the resulting scheme is only accurate in the small Mach number limit.

A Taylor expansion is performed on the particle populations in order to quantify discrete lattice effects,

$$\begin{aligned} f_i(x_\alpha + \Delta x_\alpha, t + \Delta t) = f_i(x_\alpha, t) &+ \Delta t \partial_t f_i(x_\alpha, t) \\ &+ \frac{\Delta t^2}{2}\partial_t \partial_t f_i(x_\alpha, t) + \frac{\Delta t}{Cr}\partial_\alpha c_{i\alpha} f_i(x_\alpha, t) \\ &+ \frac{\Delta t^2}{Cr^2}\frac{1}{2}\partial_\alpha \partial_\beta c_{i\alpha} c_{i\beta} f_i(x_\alpha, t) \\ &+ \frac{\Delta t^2}{Cr}\partial_t \partial_\alpha c_{i\alpha} f_i(x_\alpha, t) + \mathcal{O}\left(\epsilon^3\right). \end{aligned} \tag{A.9}$$

Time and space indices are henceforth dropped, writing $f_i = f_i(x_\alpha, t)$. Summation limits are also dropped. Summing the Taylor expansion of the time advancement equation Eq. (A.1) over all directions results in,

$$\begin{aligned} \Delta t \partial_t \sum f_i + \Delta t^2 \frac{1}{2}\partial_t \partial_t \sum f_i + \Delta t \partial_\alpha \sum c_{i\alpha} f_i \\ + \frac{\Delta t^2}{Cr}\frac{1}{2}\partial_\alpha \partial_\beta \sum c_{i\alpha} c_{i\beta} f_i + \frac{\Delta t^2}{Cr}\partial_t \partial_\alpha \sum c_{i\alpha} f_i = 0. \end{aligned} \tag{A.10}$$

Definitions from Eq. (A.5) are used to simplify,

$$\begin{aligned} \partial_t \rho + \frac{\Delta t}{2}\partial_t \partial_t \rho + \partial_\alpha \rho u_\alpha + \frac{\Delta t}{Cr}\frac{1}{2}\partial_\alpha \partial_\beta \sum c_{i\alpha} c_{i\beta} f_i \\ + \frac{\Delta t}{Cr}\partial_t \partial_\alpha \rho u_\alpha = 0. \end{aligned}$$

Substituting in the multi-scale expansions and collecting terms of order ϵ results in the conservation of mass equation,

$$\partial_{t_1} \rho + \partial_{\alpha_1} \rho u_\alpha = 0. \tag{A.11}$$

Collecting terms of order ϵ^2,

$$\partial_{t_2} \rho + \frac{\Delta t}{2}\partial_{t_1} \partial_{t_1} \rho + \frac{\Delta t}{Cr}\frac{1}{2}\partial_{\alpha_1} \partial_{\beta_1} \sum c_{i\alpha} c_{i\beta} f_i^{eq} + \frac{\Delta t}{Cr}\partial_{t_1} \partial_{\alpha_1} \rho u_\alpha = 0. \tag{A.12}$$

The conservation of mass equation at order ϵ^2 is shown to be equal to zero.

Repeating the process for the time advancement multiplied by momentum gives,

$$\begin{aligned} \Delta t \partial_t \sum c_{i\alpha} f_i + \Delta t^2 \frac{1}{2}\partial_t \partial_t \sum c_{i\alpha} f_i + \Delta t \partial_\beta \sum c_{i\alpha} c_{i\beta} f_i \\ + \frac{\Delta t^2}{Cr}\frac{1}{2}\partial_\beta \partial_\gamma \sum c_{i\alpha} c_{i\beta} c_{i\gamma} f_i + \frac{\Delta t^2}{Cr}\partial_t \partial_\beta \sum c_{i\alpha} c_{i\beta} f_i = 0 \end{aligned} \tag{A.13}$$

Definitions from Eq. (A.5) are used to simplify once again,

$$\begin{aligned} \partial_t \rho u_\alpha + \frac{\Delta t}{2}\partial_t \partial_t \rho u_\alpha + \partial_\beta \sum c_{i\alpha} c_{i\beta} f_i + \frac{\Delta t}{Cr}\frac{1}{2}\partial_\beta \partial_\gamma \sum c_{i\alpha} c_{i\beta} c_{i\gamma} f_i \\ + \frac{\Delta t}{Cr}\partial_t \partial_\beta \sum c_{i\alpha} c_{i\beta} f_i = 0 \end{aligned} \tag{A.14}$$

Substituting in the multi-scale expansions and collecting terms of order ϵ results in the following equation,

$$\partial_{t_1} \rho u_\alpha + \partial_{\beta_1} \sum c_{i\alpha} c_{i\beta} f_i^{eq} = 0. \tag{A.15}$$

Substituting the correct form of the second order equilibrium moments,

$$\sum c_{i\alpha} c_{i\beta} f_i^{eq} = c_s^2 \delta_{\alpha\beta} \rho + \rho u_\alpha u_\beta,$$

results in the pressure and advection terms in the Navier-Stokes equations,

$$\partial_{t_1} \rho u_\alpha + c_s^2 \partial_{\alpha_1} \rho + \partial_{\beta_1} \rho u_\alpha u_\beta = 0, \tag{A.16}$$

where the pressure is defined in a quasi-incompressible manner as $P = c_s^2 \rho$.

The equations at order ϵ^2 are considered next. Combining Eqs. (A.15), (A.11) and (A.12) leads to,

$$\begin{aligned} &\partial_{t_2} \rho + \frac{\Delta t}{2}\partial_{t_1} \partial_{t_1} \rho + \frac{\Delta t}{Cr}\frac{1}{2}\partial_{t_1} \partial_{\alpha_1} \rho u_\alpha = 0 \\ &\partial_{t_2} \rho + \frac{\Delta t}{2}\left(1 - \frac{1}{Cr}\right)\partial_{t_1} \partial_{t_1} \rho = 0. \end{aligned} \tag{A.17}$$

When $Cr = 1$ this results in incompressible flow with,

$$\partial_t \rho = 0 \quad \text{and} \quad \partial_\alpha \rho u_\alpha = 0.$$

Other values, with $Cr < 1$ result in solutions where any initial density perturbation field exponentially decays leaving only the incompressible solution.

The momentum equation at order ϵ^2 is,

$$\begin{aligned} \partial_{t_2} \rho u_\alpha + \frac{\Delta t}{2}\partial_{t_1} \partial_{t_1} \rho u_\alpha + \partial_{\beta_1} \sum c_{i\alpha} c_{i\beta} f_i^{(1)} \\ + \frac{\Delta t}{Cr}\frac{1}{2}\partial_{\beta_1} \partial_{\gamma_1} \sum c_{i\alpha} c_{i\beta} c_{i\gamma} f_i^{eq} + \frac{\Delta t}{Cr}\partial_{t_1} \partial_{\beta_1} \sum c_{i\alpha} c_{i\beta} f_i^{eq} = 0. \end{aligned} \tag{A.18}$$

Combining with Eq. (A.15) leads to,

$$\begin{aligned} \partial_{t_2} \rho u_\alpha + \Delta t\left(\frac{1}{Cr} - \frac{1}{2}\right)\partial_{t_1} \partial_{\beta_1} \sum c_{i\alpha} c_{i\beta} f_i^{eq} \\ + \partial_{\beta_1} \sum c_{i\alpha} c_{i\beta} f_i^{(1)} + \frac{\Delta t}{Cr}\frac{1}{2}\partial_{\beta_1} \partial_{\gamma_1} \sum c_{i\alpha} c_{i\beta} c_{i\gamma} f_i^{eq} = 0. \end{aligned} \tag{A.19}$$

An expression for the first non-equilibrium part of the particle distribution $f^{(1)}$ is required.

A Taylor expansion is performed on Eq. (A.1) without any summation,

$$\begin{aligned} \Delta t \partial_t f_i + \frac{\Delta t^2}{2}\partial_t \partial_t f_i + \Delta t \partial_\alpha c_{i\alpha} f_i + \frac{\Delta t^2}{Cr}\frac{1}{2}\partial_\alpha \partial_\beta c_{i\alpha} c_{i\beta} f_i \\ + \frac{\Delta t^2}{Cr}\partial_t \partial_\alpha c_{i\alpha} f_i = \Delta t \Omega_i \end{aligned}$$

Terms of order ϵ give,

$$\partial_{t_1} f_i^{eq} + \partial_{\alpha_1} c_{i\alpha} f_i^{eq} = \sum_{j=0}^{q} A_{ij} f_j^{(1)}.$$

Assuming the matrix A_{ij} is invertible,

$$f_i^{(1)} = \sum_{j=0}^{q} A_{ij}^{-1}\left[\partial_{t_1} f_j^{eq} + \partial_{\alpha_1} c_{j\alpha} f_j^{eq}\right],$$

Combining this expression for the off-equilibrium term with Eq (A.19) gives,

$$\begin{aligned} \partial_{t_2} \rho u_\alpha + \Delta t\left(\frac{1}{Cr} - \frac{1}{2}\right)\partial_{t_1} \partial_{\beta_1} \sum c_{i\alpha} c_{i\beta} f_i^{eq} \\ + \partial_{t_1} \partial_{\beta_1} \sum_{i=0}^{q} f_i^{eq} \sum_{j=0}^{q} A_{ij}^{-1} c_{j\alpha} c_{j\beta} \\ + \frac{\Delta t}{2Cr}\partial_{\beta_1} \partial_{\gamma_1} \sum_{i=0}^{q} c_{i\alpha} c_{i\beta} c_{i\gamma} f_i^{eq} \end{aligned}$$

$$+\partial_{\beta_1}\partial_{\gamma_1}\sum_{i=0}^{q} c_{i\gamma} f_i^{eq} \sum_{j=0}^{q} A_{ij}^{-1} c_{j\alpha} c_{j\beta} = 0. \tag{A.20}$$

Assuming that $c_{j\alpha}$ $c_{j\beta}$ are eigenvectors of the collision matrix, with eigenvalues λ then the equation can be simplified,

$$\partial_{t_2}\rho u_\alpha + \left(\frac{\Delta t}{Cr} - \frac{\Delta t}{2} + \frac{1}{\lambda}\right)\cdot \partial_{t_1}\partial_{\beta_1}\sum c_{i\alpha}c_{i\beta}f_i^{eq} + \left(\frac{\Delta t}{2Cr} + \frac{1}{\lambda}\right)\partial_{\beta_1}\partial_{\gamma_1}\sum c_{i\alpha}c_{i\beta}c_{i\gamma}f_i^{eq} = 0. \tag{A.21}$$

Time derivatives are recast as space derivatives and calculus identities are applied to equate,

$$\begin{aligned}
\partial_{t_1}\sum c_{i\alpha}c_{i\beta}f_i^{eq} &= \partial_{t_1}\left(c_s^2\rho\delta_{\alpha\beta} + \rho u_\alpha u_\beta\right),\\
&= -c_s^2\delta_{\alpha\beta}\partial_{\gamma_1}\rho u_\gamma + u_\alpha u_\beta\partial_{\gamma_1}\rho u_\gamma + u_\alpha\partial_{t_1}\rho u_\beta\\
&\quad + u_\beta\partial_{t_1}\rho u_\alpha,\\
&= -c_s^2\delta_{\alpha\beta}\partial_{\gamma_1}\rho u_\gamma + u_\alpha u_\beta\partial_{\gamma_1}\rho u_\gamma\\
&\quad + u_\alpha\left(-c_s^2\partial_{\beta_1}\rho - \partial_{\gamma_1}\rho u_\beta u_\gamma\right)\\
&\quad + u_\beta\left(-c_s^2\partial_{\alpha_1}\rho - \partial_{\gamma_1}\rho u_\alpha u_\gamma\right),\\
&= -c_s^2\left(\delta_{\alpha\beta}\partial_{\gamma_1}\rho u_\gamma + u_\alpha\partial_{\beta_1}\rho + u_\beta\partial_{\alpha_1}\rho\right)\\
&\quad - \partial_{\gamma_1}\rho u_\alpha u_\beta u_\gamma.
\end{aligned} \tag{A.22}$$

The correct form that the third order equilibrium moments must take in order to produce hydrodynamic behaviour is,

$$\sum c_{i\alpha}c_{i\beta}c_{i\gamma}f_i^{eq} = c_s^2\left(\delta_{\alpha\beta}\delta_{\gamma\delta} + \delta_{\alpha\gamma}\delta_{\beta\delta} + \delta_{\alpha\delta}\delta_{\beta\gamma}\right)\rho u_\delta + \rho u_\alpha u_\beta u_\gamma. \tag{A.23}$$

Thus,

$$\partial_{\gamma_1}\sum c_{i\alpha}c_{i\beta}c_{i\gamma}f_i^{eq} = c_s^2\left(\delta_{\alpha\beta}\partial_{\gamma_1}\rho u_\gamma + \partial_{\alpha_1}\rho u_\beta + \partial_{\beta_1}\rho u_\alpha\right) + \partial_{\gamma_1}\rho u_\alpha u_\beta u_\gamma.$$

Summing the second and third moment terms gives,

$$\partial_{t_1}\sum c_{i\alpha}c_{i\beta}f_i^{eq} + \partial_{\gamma_1}\sum c_{i\alpha}c_{i\beta}c_{i\gamma}f_i^{eq} = c_s^2\rho\left(\partial_{\alpha_1}u_\beta + \partial_{\beta_1}u_\alpha\right),$$

which correctly models viscous momentum flux terms in the Navier-Stokes equations.

The exact relationship between the mixed time and space derivative of second order moments and the space derivative of third order moments demonstrated above allows the density to be moved outside of the spatial derivative in viscous terms,

$$\partial_\alpha\rho u_\beta + \partial_\beta\rho u_\alpha = \rho\left(\partial_\alpha u_\beta + \partial_\beta u_\alpha\right) + u_\beta\partial_\alpha\rho + u_\alpha\partial_\beta\rho. \tag{A.24}$$

This part of the analysis can be simplified if terms of order Ma^2 are neglected and grouped with other error terms without degrading the order of accuracy since these quasi-incompressible LB methods are only accurate in the small Mach number limit where density fluctuations $\partial_t\rho$ approach zero. These density variations, which are of order Ma^2 [52,63], are treated as error terms,

$$\partial_t\rho = \partial_\alpha\rho u_\alpha = \mathcal{O}\left(\mathrm{Ma}^2\right).$$

Spatial density variations are also of the same order,

$$\rho_0\partial_t u_\alpha \sim -c_s^2\partial_\alpha\rho \;\rightarrow\; u_\beta\partial_\alpha\rho \sim -u_\beta\rho_0\frac{\partial_t u_\alpha}{c_s^2} \sim \mathcal{O}\left(\mathrm{Ma}^2\right)$$

This means that the terms that arise when density variations are moved outside of derivatives in Eq. A.24 can be neglected,

$$\partial_\alpha\rho u_\beta + \partial_\beta\rho u_\alpha = \rho\left(\partial_\alpha u_\beta + \partial_\beta u_\alpha\right) + \mathcal{O}\left(\mathrm{Ma}^2\right).$$

This can be repeated,

$$\partial_\beta\rho\partial_\beta u_\alpha = \partial_\beta u_\alpha\cdot\partial_\beta\rho + \rho\partial_\beta\partial_\beta u_\alpha = \rho\partial_\beta\partial_\beta u_\alpha + \mathcal{O}\left(\mathrm{Ma}^2\right).$$

The velocity cubed term in the third order equilibrium moments shown in Eq A.23 can similarly be neglected without degrading the order of accuracy. This is important since many commonly used lattices lack sufficient degrees of freedom to correctly set the velocity cubed equilibrium moments.

$$u_\alpha < \mathrm{Ma} < 1 \;\rightarrow\; u_\alpha u_\beta u_\gamma < \mathrm{Ma}^2$$

The simplified version of Eq A.22 is,

$$\partial_{t_1}\sum c_{i\alpha}c_{i\beta}f_i^{eq} = -c_s^2\delta_{\alpha\beta}\partial_{\gamma_1}\rho u_\gamma + \mathcal{O}\left(\mathrm{Ma}^2\right) = \mathcal{O}\left(\mathrm{Ma}^2\right).$$

Combining the simplified terms and grouping terms of order Ma^2, Eq. A.20 is found to be equal to the viscous terms of the Navier-Stokes momentum equations,

$$\partial_{t_2}\rho u_\alpha + c_s^2\left(\frac{\Delta t}{2Cr} + \frac{1}{\lambda}\right)\rho\partial_\beta\partial_\beta u_\alpha = \mathcal{O}\left(\mathrm{Ma}^2\right).$$

The viscosity is specified by adjusting the eigenvalues λ,

$$\nu = -c_s^2\left(\frac{\Delta t}{2Cr} + \frac{1}{\lambda}\right).$$

For example, using the common single relaxation time collision operator, the relaxation parameter is chosen to be $\omega = -\lambda$. The quasi-incompressible Navier-Stokes equations that are modelled are written out in full,

$$\partial_\alpha\rho u_\alpha = \mathcal{O}\left(\mathrm{Ma}^2\right)$$

$$\partial_t\rho u_\alpha + \partial_\beta\rho u_\alpha u_\beta = -c_s^2\partial_\alpha\rho + \nu\rho\partial_\beta\partial_\beta u_\alpha + \mathcal{O}\left(\mathrm{Ma}^2\right).$$

References

[1] Obrecht C, Kuznik F, Tourancheau B, Roux JJ. Multi-GPU implementation of a hybrid thermal lattice Boltzmann solver using the TheLMA framework. Comput Fluids 2013;80:269–75.

[2] Zecevic V, Kirkpatrick MP, Armfield SW. The lattice Boltzmann method for turbulent channel flows using graphics processing units. In: Proceedings of the 15th Biennial Computational Techniques and Applications Conference, CTAC-2010, Vol. 52 of ANZIAM J.; 2011. p. C914–31.

[3] Xian W, Takayuki A. Multi-GPU performance of incompressible flow computation by lattice Boltzmann method on GPU cluster. Parallel Comput 2011;37:521–35.

[4] Toelke J, Krafczyk M. TeraFLOP computing on a desktop PC with GPUs for 3D CFD. Int J Comput Fluid Dyn 2008;22:443–56.

[5] Premnath KN, Pattison MJ, Banerjee S. Generalized lattice Boltzmann equation with forcing term for computation of wall-bounded turbulent flows. Phys Rev E 2009;79.

[6] Patil DV, Lakshmisha KN. Finite volume TVD formulation of lattice Boltzmann simulation on unstructured mesh. J Comput Phys 2009;228:5262–79.

[7] Obrecht C, Kuznik F, Tourancheau B, Roux J. The TheLMA project: a thermal lattice Boltzmann solver for the GPU. Comput Fluids 2012;54:118–26.

[8] Chen S, Doolen GD. Lattice Boltzmann method for fluid flows. Annu Rev Fluid Mech 1998;30:329–64.

[9] Aidun CK, Clausen JR. Lattice Boltzmann method for complex flows. Annu Rev Fluid Mech 2010;42:439–72.

[10] Wolf-Gladrow DA. Lattice-gas cellular automata and lattice Boltzmann models - an Introduction, Vol. 1725 of Lect. notes math. Berlin: Springer; 2000.

[11] Succi S. The lattice Boltzmann equation for fluid dynamics and beyond. Oxford University Press; 2001.

[12] Nannelli F, Succi S. The lattice Boltzmann equation on irregular lattices. J Stat Phys 1992;68:401–7.

[13] Peng GW, Xi HW, Duncan C, Chou SH. Lattice Boltzmann method on irregular meshes. Phys Rev E 1998;58:R4124–7.

[14] Ubertini S, Succi S, Bella G. Lattice Boltzmann schemes without coordinates. Philos Trans R Soc A - Math Phys Eng Sci 2004;362:1763–71.

[15] Lee T, Lin CL. A characteristic Galerkin method for discrete Boltzmann equation. J Comput Phys 2001;171:336–56.

[16] Lee T, Lin C. An Eulerian description of the streaming process in the lattice Boltzmann equation. J Comput Phys 2003;185:445–71.

[17] Bardow A, Karlin IV, Gusev AA. General characteristic-based algorithm for off-lattice Boltzmann simulations. Europhys Lett 2006;75:434–40.

[18] Min M, Lee T. A spectral-element discontinuous Galerkin lattice Boltzmann method for nearly incompressible flows. J Comput Phys 2011;230:245–59.

[19] Cao N, Chen S, Jin S, Martinez D. Physical symmetry and lattice symmetry in the lattice Boltzmann method. Phys Rev E 1997;55:R21–4.

[20] Guo ZL, Zhao TS. Explicit finite-difference lattice Boltzmann method for curvilinear coordinates. Phys Rev E 2003;67.

[21] Tamura A, Okuyama K, Takahashi S, Ohtsuka M. Three-dimensional discrete-velocity BGK model for the incompressible Navier-Stokes equations. Comput Fluids 2011;40:149–55.
[22] Hejranfar K, Hajihassanpour M. Chebyshev collocation spectral lattice Boltzmann method in generalized curvilinear coordinates. Comput Fluids 2017;146:154–73.
[23] He XY, Doolen GD. Lattice Boltzmann method on a curvilinear coordinate system: Vortex shedding behind a circular cylinder. Phys Rev E 1997;56:434–40.
[24] He XY, Luo LS, Dembo M. Some progress in lattice Boltzmann method. 1. Nonuniform mesh grids. J Comput Phys 1996;129:357–63.
[25] Dixit HN, Babu V. Simulation of high Rayleigh number natural convection in a square cavity using the lattice Boltzmann method. Int J Heat Mass Transf 2006;49:727–39.
[26] Shu C, Chew YT, Niu XD. Least-squares-based lattice Boltzmann method: A meshless approach for simulation of flows with complex geometry. Phys Rev E 2001;64.
[27] Kuznik F, Vareilles J, Rusaouen G, Krauss G. A double-population lattice Boltzmann method with non-uniform mesh for the simulation of natural convection in a square cavity. Int J Heat Fluid Flow 2007;28:862–70.
[28] Filippova O, Hanel D. Grid refinement for lattice-BGK models. J Comput Phys 1998;147:219–28.
[29] Stiebler M, Toelke J, Krafczyk M. Advection-diffusion lattice Boltzmann scheme for hierarchical grids. Comput Math Appl 2008;55:1576–84.
[30] Lagrava D, Malaspinas O, Latt J, Chopard B. Advances in multi-domain lattice Boltzmann grid refinement. J Comput Phys 2012;231:4808–22.
[31] Rohde M, Kandhai D, Derksen JJ, van den Akker HEA. A generic, mass conservative local grid refinement technique for lattice-Boltzmann schemes. Int J Numer Methods Fluids 2006;51:439–68.
[32] Karlin IV, Succi S, Orszag S. Lattice Boltzmann method for irregular grids. Phys Rev Lett 1999;82:5245–8.
[33] Bouzidi M, d'Humieres D, Lallemand P, Luo LS. Lattice Boltzmann equation on a two-dimensional rectangular grid. J Comput Phys 2001;172:704–17.
[34] Zhou JG. Rectangular lattice Boltzmann method. Phys Rev E 2010;81.
[35] Zhou JG. MRT rectangular lattice Boltzmann method. Int J Mod Phys C 2012;23.
[36] Ren J, Guo P, Guo Z. Rectangular lattice Boltzmann equation for gaseous microscale flow. Adv Appl Math Mech 2016;8:306–30.
[37] HegelerJr LA, Mattila K, Philippi PC. Rectangular lattice-Boltzmann schemes with BGK-collision operator. J Sci Comput 2013;56:230–42.
[38] Peng C, Min H, Guo Z, Wang LP. A hydrodynamically-consistent MRT lattice Boltzmann model on a 2D rectangular grid. J Comput Phys 2016;326:893–912.
[39] He XY, Luo LS. Lattice Boltzmann model for the incompressible Navier-Stokes equation. J Stat Phys 1997;88:927–44.
[40] Kandhai D, Koponen A, Hoekstra A, Kataja M, Timonen J, Sloot PMA. Implementation aspects of 3D lattice-BGK: boundaries, accuracy, and a new fast relaxation method. J Comput Phys 1999;150:482–501.
[41] Lallemand P, Luo LS. Theory of the lattice Boltzmann method: Dispersion, dissipation, isotropy, Galilean invariance, and stability. Phys Rev E 2000;61:6546–62.
[42] d'Humieres D, Bouzidi M, Lallemand P. Thirteen-velocity three-dimensional lattice Boltzmann model. Phys Rev E 2001;63.
[43] Dellar P. Incompressible limits of lattice Boltzmann equations using multiple relaxation times. J Comput Phys 2003;190:351–70.
[44] Moser RD, Kim J, Mansour NN. Direct numerical simulation of turbulent channel flow up to Re_τ =590. Phys Fluids 1999;11:943–5.
[45] Ginzbourg I, Adler PM. Boundary flow condition analysis for the 3-dimensional lattice Boltzmann model. J Phys II 1994;4:191–214.
[46] Zecevic V, Kirkpatrick MP, Armfield SW. Stability and accuracy of various difference schemes for the lattice Boltzmann method. In: Proceedings of the 10th Biennial Engineering Mathematics and Applications Conference, EMAC-2011, Vol. 53 of ANZIAM J.; 2012. p. C494–510.
[47] Frisch U, d'Humieres D, Hasslacher B, Lallemand P, Pomeau Y, Rivet JP. Lattice gas hydrodynamics in two and three dimensions. Complex Syst 1987;1:649–707.
[48] Karlin I, Asinari P. Factorization symmetry in the lattice Boltzmann method. Physica A 2010;389:1530–48.
[49] Yasuda T, Hashimoto T, Tanno I, Tanaka Y, Minagawa H, Morinishi K, Satofuka N. Effect of collision and velocity model of lattice Boltzmann model on three-dimensional turbulent flow simulation. Int J Comput Fluid Dyn 2017;31:258–68.
[50] Chikatamarla SS, Karlin IV. Comment on "Rectangular lattice Boltzmann method". Phys Rev E 2011;83.
[51] d'Humieres D, Ginzburg I, Krafczyk M, Lallemand P, Luo LS. Multiple-relaxation-time lattice Boltzmann models in three dimensions. Philos Trans R Soc A - Math Phys Eng Sci 2002;360:437–51.
[52] Sterling JD, Chen SY. Stability analysis of lattice Boltzmann methods. J Comput Phys 1996;123:196–206.
[53] Rheinlaender M. On the stability structure for lattice Boltzmann schemes. Comput Math Appl 2010;59:2150–67.
[54] Brownlee RA, Gorban AN, Levesley J. Stability and stabilization of the lattice Boltzmann method. Phys Rev E 2007;75.
[55] Latt J, Chopard B. Lattice Boltzmann method with regularized pre-collision distribution functions. Math Comput Simul 2006;72:165–8.
[56] Banda MK, Yong WA, Klar A. A stability notion for lattice Boltzmann equations. SIAM J Sci Comput 2006;27:2098–111.
[57] Qian YH. Fractional propagation and the elimination of staggered invariants in lattice-BGK models. Int J Mod Phys C 1997;8:753–61.
[58] Skordos PA. Initial and boundary conditions for the lattice Boltzmann method. Phys Rev E 1993;48:4823–42.
[59] Caiazzo A. Analysis of lattice Boltzmann initialization routines. J Stat Phys 2005;121:37–48.
[60] Mei R, Luo LS, Lallemand P, d'Humieres D. Consistent initial conditions for lattice Boltzmann simulations. Comput Fluids 2006;35(8-9):855–62.
[61] Guo ZL, Zheng CG, Shi BC. Discrete lattice effects on the forcing term in the lattice Boltzmann method. Phys Rev E 2002;65.
[62] Reider MB, Sterling JD. Accuracy of discrete-velocity BGK models for the simulation of the incompressible Navier-Stokes equations. Comput Fluids 1995;24:459–67.
[63] Martinez DO, Matthaeus WH, Chen S, Montgomery DC. Comparison of spectral method and lattice Boltzmann simulations of 2-dimensional hydrodynamics. Phys Fluids 1994;6:1285–98.